ALESS-JWST: Joint (Sub)kiloparsec JWST and ALMA Imaging of z □ 3 Submillimeter Galaxies Reveals Heavily Obscured Bulge

The Astrophysical Journal, 978:165 (20pp), 2025 January 10 https://doi.org/10.3847/1538-4357/ad9a52

ALESS-JWST: Joint (Sub)kiloparsec JWST and ALMA Imaging of $z \sim 3$ Submillimeter Galaxies Reveals Heavily Obscured Bulge Formation Events

J. A. Hodge[1], E. da Cunha[2,3], S. Kendrew[4], J. Li[2], I. Smail[5], B. A. Westoby[1], O. Nayak[4,6], A. M. Swinbank[5], C.-C. Chen[7], F. Walter[8], P. van der Werf[1], M. Cracraft[9], A. Battisti[2,3,10], W. N. Brandt[11,12,13], G. Calistro Rivera[14,15], S. C. Chapman[16,17,18,19], P. Cox[20], H. Dannerbauer[21], R. Decarli[22], M. Frias Castillo[1], T. R. Greve[23,24,25], K. K. Knudsen[26], S. Leslie[1], K. M. Menten[27], M. Rybak[1,28,29], E. Schinnerer[8], J. L. Wardlow[30], and A. Weiss[27]

[1] Leiden Observatory, Leiden University, P.O. Box 9513, 2300 RA Leiden, The Netherlands; hodge@strw.leidenuniv.nl
[2] International Centre for Radio Astronomy Research, University of Western Australia, 35 Stirling Highway, Crawley 26WA 6009, Australia
[3] ARC Centre of Excellence for All Sky Astrophysics in 3 Dimensions (ASTRO 3D), Australia
[4] European Space Agency (ESA), ESA Office, Space Telescope Science Institute, 3700 San Martin Drive, Baltimore, MD 21218, USA
[5] Centre for Extragalactic Astronomy, Department of Physics, Durham University, South Road, Durham DH1 3LE, UK
[6] NASA Goddard Space Flight Center, 8800 Greenbelt Road, Greenbelt, MD, USA
[7] Academia Sinica Institute of Astronomy and Astrophysics (ASIAA), No. 1, Sec. 4, Roosevelt Road, Taipei 106216, Taiwan
[8] Max–Planck Institut für Astronomie, Königstuhl 17, 69117 Heidelberg, Germany
[9] Space Telescope Science Institute, 3700 San Martin Drive, Baltimore, MD 21218, USA
[10] Research School of Astronomy and Astrophysics, Australian National University, Cotter Road, Weston Creek, ACT 2611, Australia
[11] Department of Astronomy and Astrophysics, 525 Davey Lab, The Pennsylvania State University, University Park, PA 16802, USA
[12] Institute for Gravitation and the Cosmos, The Pennsylvania State University, University Park, PA 16802, USA
[13] Department of Physics, 104 Davey Laboratory, The Pennsylvania State University, University Park, PA 16802, USA
[14] German Aerospace Center (DLR), Institute of Communications and Navigation, Wessling, Germany
[15] European Southern Observatory (ESO), Karl-Schwarzschild-Straße 2, 85748 Garching bei Müunchen, Germany
[16] Department of Physics and Atmospheric Science, Dalhousie University, 6310 Coburg Road, B3H 4R2, Halifax, Canada
[17] National Research Council, Herzberg Astronomy and Astrophysics, 5071 West Saanich Road, Victoria, V9E 2E7, Canada
[18] Department of Physics and Astronomy, University of British Columbia, 6225 Agricultural Road, Vancouver, V6T 1Z1, Canada
[19] Eureka Scientific Inc., Oakland, CA 94602, USA
[20] Sorbonne Université, UPMC Université Paris 6 and CNRS, UMR 7095, Institut d'Astrophysique de Paris, 98bis boulevard Arago, 75014 Paris, France
[21] Instituto de Astrofísica de Canarias, Vía Láctea, 39020 La Laguna (Tenerife), Spain
[22] INAF – Osservatorio di Astrofisica e Scienza dello Spazio di Bologna, via Gobetti 93/3, I-40129, Bologna, Italy
[23] Cosmic Dawn Center (DAWN), Denmark
[24] DTU Space, Technical University of Denmark, Elektrovej, Building 328, 2800, Kgs. Lyngby, Denmark
[25] Dept. of Physics and Astronomy, University College London, Gower Street, London WC1E 6BT, UK
[26] Department of Space, Earth and Environment, Chalmers University of Technology, SE-412 96 Gothenburg, Sweden
[27] Max-Planck-Institut für Radioastronomie, Auf dem Hügel 69, D-53121 Bonn, Germany
[28] Faculty of Electrical Engineering, Mathematics and Computer Science, Delft University of Technology, Mekelweg 4, 2628 CD Delft, The Netherlands
[29] SRON–Netherlands Institute for Space Research, Niels Bohrweg 4, 2333 CA Leiden, The Netherlands
[30] Department of Physics, Lancaster University, Lancaster, LA1 4YB, UK
Received 2024 July 22; revised 2024 November 15; accepted 2024 November 17; published 2025 January 10

Abstract

We present JWST NIRCam imaging targeting 13 $z \sim 3$ infrared-luminous ($L_{\rm IR} \sim 5 \times 10^{12} L_{\odot}$) galaxies from the ALESS survey with uniquely deep, high-resolution (0.″08–0.″16) Atacama Large Millimeter/submillimeter Array 870 μm imaging. The 2.0–4.4 μm (observed frame) NIRCam imaging reveals the rest-frame near-infrared stellar emission in these submillimeter-selected galaxies at the same (sub)kiloparsec resolution as the 870 μm dust continuum. The newly revealed stellar morphologies show striking similarities with the dust continuum morphologies at 870 μm, with the centers and position angles agreeing for most sources, clearly illustrating that the spatial offsets reported previously between the 870 μm and Hubble Space Telescope morphologies were due to strong differential dust obscuration. The F444W sizes are 78% ± 21% larger than those measured at 870 μm, in contrast to recent results from hydrodynamical simulations that predict larger 870 μm sizes. We report evidence for significant dust obscuration in F444W for the highest-redshift sources, emphasizing the importance of longer-wavelength MIRI imaging. The majority of the sources show evidence that they are undergoing mergers/interactions, including tidal tails/plumes—some of which are also detected at 870 μm. We find a clear correlation between NIRCam colors and 870 μm surface brightness on ∼1 kpc scales, indicating that the galaxies are primarily red due to dust—not stellar age—and we show that the dust structure on ∼kpc scales is broadly similar to that in nearby galaxies. Finally, we find no strong stellar bars in the rest-frame near-infrared, suggesting the extended bar-like features seen at 870 μm are highly obscured and/or gas-dominated structures that are likely early precursors to significant bulge growth.

Unified Astronomy Thesaurus concepts: High-redshift galaxies (734)

1. Introduction

With the advent of the first infrared (IR) sky surveys, including by IRAS (G. Neugebauer et al. 1984) and COBE (J. C. Mather 1994), a basic fact of the Universe was revealed: roughly half of the star formation that has occurred over cosmic time took place shrouded behind cosmic dust (e.g., J. L. Puget et al. 1996; M. G. Hauser et al. 1998). Thanks to the decades of dedicated follow-up that subsequently occurred in order to systematically resolve the IR/submillimeter background, we now know that this dust-obscured star formation was as important as unobscured star formation at least out to $z \sim 4$ (e.g., R. Bouwens et al. 2020; U. Dudzevičiutė et al. 2020; J. A. Zavala et al. 2021), and perhaps even beyond (e.g., H. S. B. Algera et al. 2023). The galaxies with the most significant dust-obscured star formation rates are the $z \sim$ 2–5 galaxies discovered in the earliest single-dish submillimeter surveys (SMGs; e.g., I. Smail et al. 1997; A. J. Barger et al. 1998; D. H. Hughes et al. 1998; S. Eales et al. 1999). Canonically, SMGs are thought to be tied to the evolution of QSOs (e.g., D. B. Sanders & I. F. Mirabel 1996; P. F. Hopkins et al. 2006) and ultimately to the buildup of massive elliptical galaxies (e.g., I. Smail et al. 2004; A. M. Swinbank et al. 2006; A. Cimatti et al. 2008; P. G. van Dokkum et al. 2008; J. M. Simpson et al. 2014; S. Toft & B. Magnelli 2014; and see C. M. Casey et al. 2014 for a review). Understanding the physical processes that drove their intense dusty star formation is thus crucial for understanding massive galaxy evolution.

Prior to the launch of the James Webb Space Telescope (JWST), characterizing the stellar counterparts of SMGs was notoriously difficult. While many SMGs can be detected with Spitzer IRAC in at least one band (e.g., D. Iono et al. 2006; W.-H. Wang et al. 2007; S. Ikarashi et al. 2011; W.-H. Wang et al. 2011; J. M. Simpson et al. 2014), its relatively poor spatial resolution makes morphological studies impossible. Meanwhile, studies using, e.g., deep Hubble Space Telescope (HST) H-band imaging report conflicting results on the prevalence of merger activity (e.g., A. M. Swinbank et al. 2010; T. A. Targett et al. 2013; C.-C. Chen et al. 2015). However, these dust-rich galaxies are particularly prone to structured dust extinction (e.g., J. M. Simpson et al. 2017; R. K. Cochrane et al. 2019), suggesting their rest-frame UV/optical classifications may be unreliable (e.g., P. Lang et al. 2019; G. Popping et al. 2022). Moreover, such studies also report high fractions of near-IR (NIR)-faint sources ($\sim$20% at $m_{\rm H} \sim 27.8$ mag depth; C.-C. Chen et al. 2015), presumably due to their high levels of dust attenuation (median global $A_{\rm V} \sim$ 2–3 mag; E. da Cunha et al. 2015; U. Dudzevičiutė et al. 2020), precluding reliable morphological classification. Finally, even for the sources detected with, e.g., HST, their stellar masses typically carry large uncertainties due to the well-known degeneracy between stellar age and dust attenuation (e.g., L. J. Hainline et al. 2011; M. J. Michałowski et al. 2014; U. Dudzevičiutė et al. 2020). These observational challenges have contributed to the lack of theoretical consensus on the nature of SMGs and the physical mechanism(s) by which their dusty star formation was triggered (e.g., C. M. Baugh et al. 2005; D. Narayanan et al. 2010, 2015; C. C. Hayward et al. 2013b; C. C. Hayward et al. 2013a; S. McAlpine et al. 2019; C. C. Lovell et al. 2021).

In the last decade, the advent of the Atacama Large Millimeter/submillimeter Array (ALMA) has provided critical new insight into dust-obscured star formation at high redshift (e.g., see J. A. Hodge & E. da Cunha 2020 for a review). In particular, ALMA (along with the Submillimeter Array, and the Northern Extended Millimeter Array) have allowed large samples of the classically single-dish-selected SMGs to be located with interferometric accuracy (e.g., J. D. Younger et al. 2008, 2009; A. J. Barger et al. 2012; V. Smolčić 2012; J. A. Hodge et al. 2013; J. M. Simpson et al. 2014; J. S. Spilker et al. 2016; R. Hill et al. 2018; S. M. Stach et al. 2019) and resolved directly in their (sub) millimeter continuum emission (e.g., J. M. Simpson et al. 2015; S. Ikarashi et al. 2015; J. A. Hodge et al. 2016; B. Gullberg et al. 2019). These studies have revealed that the (sub)millimeter continuum emission in these galaxies is relatively compact and has disk-like morphology (i.e., with a Sérsic index $n \sim 1$; e.g., J. M. Simpson et al. 2015; J. A. Hodge et al. 2016; B. Gullberg et al. 2019) and often appears spatially offset from the rest-frame UV/optical continuum (e.g., J. A. Hodge et al. 2012; C.-C. Chen et al. 2015; G. Calistro Rivera et al. 2018), which some studies have interpreted as being due to real physical offsets between the location of the dusty star formation and the bulk of the stellar mass (C.-C. Chen et al. 2015). The highest-resolution studies have further resolved the (sub)millimeter continuum-traced dust disks in small subsamples into distinct substructures on $\sim$0.5–1 kpc scales, uncovering features with morphologies suggestive of bars, rings, and (tidally induced) spiral arms (J. A. Hodge et al. 2019; see also B. Gullberg et al. 2019). Unfortunately, despite the depth of the available HST imaging, no meaningful comparison could be made to the stellar structure due to the faintness of the sources in the rest-frame UV/optical.

Recently, the launch of JWST has shed new light on the nature of submillimeter-selected sources by revealing their rest-frame near-infrared morphologies on (sub)kiloparsec scales (e.g., C.-C. Chen et al. 2022; C. Cheng et al. 2023; L. Colina et al. 2023; S. Huang et al. 2023; S. Gillman et al. 2023, 2024; L. A. Boogaard et al. 2024; A. Gómez et al. 2024). Some of these early studies have reported evidence for undisturbed, disk-like morphologies that have been taken as evidence for the importance of secular growth for their stellar mass assembly (e.g., C. Cheng et al. 2023). Other studies have also reported evidence for disk-like morphologies but with a broad scatter in the nonparametric parameter space for morphological classification (S. Gillman et al. 2023), indicating a diverse population that nevertheless reflects the field population (S. Gillman et al. 2024). A number of studies have identified structures in the rest-frame near-infrared emission akin to bulges, spiral arms, and bars (e.g., C.-C. Chen et al. 2022; S. Huang et al. 2023; I. Smail et al. 2023; A. Amvrosiadis et al. 2024), as well as examples of tidal features indicating dynamical interactions (e.g., C.-C. Chen et al. 2022; J. Cathey et al. 2024). However, given the relatively narrow-field coverage of JWST in relation to the number density of SMGs, the submillimeter-selected galaxies studied so far in extragalactic deep fields have largely constituted submillimeter-fainter sources (i.e., $\lesssim$few mJy at 850 μm), which may undergo different triggering mechanisms than the submillimeter-brighter sources (e.g., C. C. Hayward et al. 2013b). More crucially, the current samples have lacked equally high-resolution ALMA dust continuum imaging, preventing the incorporation of the (energetically important) dust continuum emission into the physical interpretation.

Here, we present multiband NIRCam imaging at 2–4.4 μm (observed-frame) of 13 $z \sim 3$ SMGs from the ALMA follow-up of the LABOCA Extended Chandra Deep Field South Survey (ALESS; J. A. Hodge et al. 2013; A. Karim et al. 2013). These submillimeter-bright (median $S_{870} \sim$ 6 mJy) galaxies all have deep ALMA 870 μm continuum imaging at 0.″08–0.″16 resolution (J. A. Hodge et al. 2016, 2019), allowing us to compare their

Table 1
Target Properties: Sample

Source ID[a]	Position[a] (J2000)	S_{870}[a] (mJy)	z[b]	Redshift Source[b]	870 μm FWHM[c]	NIRCam Pointing
ALESS 1.1	03:33:14.46 −27:56:14.5	6.7 ± 0.5	4.674	CO(5–4)	0.″16	2
ALESS 1.2	03:33:14.41 −27:56:11.6	3.5 ± 0.4	4.669	CO(5–4)	0.″16	2
ALESS 1.3	03:33:14.16 −27:56:12.5	1.9 ± 0.4	$2.86^{+0.46}_{-1.53}$	$z_{\rm phot}$	0.″16	2
ALESS 3.1	03:33:21.51 −27:55:20.5	8.3 ± 0.4	3.375	CO(5–4), CO(4–3), [CI]	0.″08	2
ALESS 9.1	03:32:11.33 −27:52:12.0	8.8 ± 0.5	3.694	CO(4–3), [CI]	0.″08	3
ALESS 10.1	03:32:19.05 −27:52:14.8	5.2 ± 0.5	$3.34^{+0.02}_{-0.16}$	$z_{\rm phot}$[d]	0.″16	3
ALESS 15.1	03:33:33.37 −27:59:29.7	9.0 ± 0.4	$2.86^{+0.10}_{-0.20}$	$z_{\rm phot}$	0.″08	1
ALESS 17.1	03:32:07.29 −27:51:20.9	8.4 ± 0.5	1.5397	H_α, CO(5–4), CO(2–1)	0.″08	3
ALESS 29.1	03:33:36.90 −27:58:09.3	5.9 ± 0.4	$3.69^{+0.42}_{-0.45}$	$z_{\rm phot}$[e]	0.″16	1
ALESS 45.1	03:32:25.26 −27:52:30.6	6.0 ± 0.5	$3.09^{+0.22}_{-0.26}$	$z_{\rm phot}$	0.″16	3
ALESS 76.1	03:33:32.35 −27:59:55.7	6.4 ± 0.6	3.3895	[O III]	0.″08	1
ALESS 112.1	03:32:48.86 −27:31:13.2	7.6 ± 0.5	2.314	Lyα, CO(3–2)	0.″08	4
ALESS 3.1-comp	03:33:21.43 −27:55:25.4	1.07 ± 0.06	3.374[f]	CO(5–4), CO(4–3)[f]	0.″08	2

Notes.
[a] Source IDs and 870 μm flux densities are from J. A. Hodge et al. (2013) except for ALESS 3.1-comp, which is newly reported here. Source positions for all sources have been updated based on the high-resolution 870 μm data available in J. A. Hodge et al. (2016, 2019).
[b] Rest-frame optical/UV-based spectroscopic redshifts are from A. L. R. Danielson et al. (2017), CO-based redshifts are from J. E. Birkin et al. (2021), and the photometric redshifts were taken from E. da Cunha et al. (2015) and updated to include the new NIRCam+MIRI photometry (J. Li et al. 2025, in preparation).
[c] Highest-resolution 870 μm continuum data available on the source. All sources with 0.″08 observations also have 0.″16 observations. For details, see Section 2.3.
[d] ALESS 10.1 was previously reported to have $z_{\rm spec} = 0.7616$ based on multiple lines in an optical spectrum (A. L. R. Danielson et al. 2017), but this was likely an incorrect identification of an unrelated foreground source based on the very red colors of the SMG, which are difficult to reconcile with such a redshift. We therefore assume its photometric redshift here.
[e] ALESS 29.1 was previously reported to have $z_{\rm spec} = 1.438$ (A. L. R. Danielson et al. 2017), but based on both its red colors (difficult to reconcile with this redshift) and the lack of a CO detection at that redshift (J. E. Birkin et al. 2021), we assume its photometric redshift here.
[f] CO-based redshift from B. Westoby et al. (2025, in preparation)

newly revealed rest-frame near-infrared emission to their dust continuum emission on the same (sub)kiloparsec scales. We begin in Section 2 by discussing the sample selection, the JWST observations and data reduction, and the existing 870 μm ALMA data. We present our analysis and results in Section 3, including a comparison between the detected stellar and dust continuum emission, a visual classification, a curve-of-growth analysis of the effective radii, GALFIT modeling, isophotal fitting to search for stellar bars, and finally a comparison of the NIRCam colors with ALMA 870 μm. We follow this with a discussion in Section 4. We end with our conclusions in Section 5. Throughout this paper, we adopt a standard spatially flat cold dark matter cosmology from the Planck 2018 results with Hubble constant $H_0 = 67.4\,{\rm km\,s^{-1}\,Mpc^{-1}}$, dark energy density parameter $\Omega_\Lambda = 0.685$, and matter density parameter $\Omega_M = 0.315$ (Planck Collaboration et al. 2020). With these parameters, 1″ corresponds to 7.9 kpc at $z \sim 3$. We adopt a G. Chabrier (2003) initial mass function and AB system magnitudes.

2. Observations and Data Reduction

2.1. Sample Selection

The JWST observations targeted 13 SMGs[31] originally detected in the LABOCA 870 μm survey of the ECDFS (A. Weiß & K. Coppin 2009) and then interferometrically identified as part of the ALESS survey (J. A. Hodge et al. 2013; A. Karim et al. 2013; J. M. Simpson et al. 2014; E. da Cunha et al. 2015; A. L. R. Danielson et al. 2017). These 13 galaxies were part of the sample subsequently followed up with high-resolution, high-fidelity ALMA 870 μm continuum mapping observations (J. A. Hodge et al. 2016, 2019; also see Section 2.3 for details). The sample is listed in Table 1. Eight of the targets have spectroscopic redshifts, also listed in Table 1; the remaining five have high-quality MAGPHYS-based photometric redshifts, which have been updated from those listed in E. da Cunha et al. (2015) to include the new JWST NIRCam+MIRI photometry (J. Li et al. 2025, in preparation; Table 1).

Due to the original selection criteria for the high-resolution ALMA 870 μm follow-up, which was based entirely on total 870 μm flux density and the availability of (effectively randomly targeted) HST coverage (C.-C. Chen et al. 2015; and we note that no selection was made on ALMA or HST morphology), the sources targeted here include some of the submillimeter-brightest sources from the ALESS parent sample: the median 870 μm flux density of the sources is 6.4 mJy, with a 16th–84th percentile range of 3.4–8.4 mJy. The galaxies nevertheless span a wide range of redshifts ($z \simeq 1.5 - 4.5$) and star formation rates (∼60–1000 $M_\odot\,{\rm yr^{-1}}$). The median redshift of the targets is 3.4, with a 16th–84th percentile range of 2.8–3.8. The median SFR is 350 $M_\odot\,{\rm yr^{-1}}$, with a 16th–84th percentile range of 190–820 $M_\odot\,{\rm yr^{-1}}$. The sample is thus slightly higher-redshift and more highly star-forming than the parent population of ALESS SMGs ($z_{\rm phot} = 2.7 \pm 0.1$ and SFR $= 280 \pm 70\,M_\odot\,{\rm yr^{-1}}$; E. da Cunha et al. 2015). Finally, only one of the sources (ALESS 45.1) may be associated with an X-ray active galactic nucleus (AGN; S. X. Wang et al. 2013; B. Luo et al. 2017; J. Lyu et al. 2022), though we caution that the conclusions of S. X. Wang et al. (2013) and B. Luo et al. (2017) differ on whether the X-ray source could be powered by star formation,

[31] The 13th SMG, ALESS 3.1-comp, was discovered by the subsequent deep 870 μm imaging (J. A. Hodge et al. 2016, 2019) near ALESS 3.1; see Section 3.1 for details.

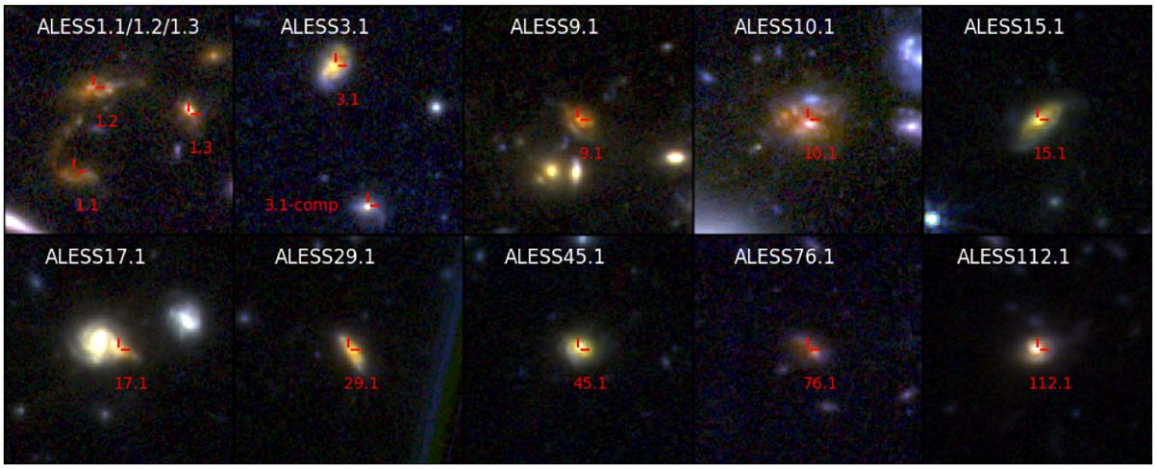

Figure 1. JWST NIRCam RGB images of $8'' \times 8''$ regions ($\sim$65 $\times$ 65 kpc at $z \sim 3$) around far-IR (FIR)-luminous SMGs from the ALMA ALESS survey. North is up and east is to the left. The RGB images were made with the F444W (red), F356W (green), and F200W (blue) NIRCam filters. The positions of the 870 μm sources are indicated with their ALESS ID numbers. All galaxies are clearly detected by NIRCam. ALESS 1.1, 1.2, and 1.3 are shown together in the same cutout. Note the long tidal tail revealed by the NIRCam imaging of ALESS 1.1/1.2, indicating an interaction. There is also an 870 μm-detected companion (3.1-comp) to the South of ALESS 3.1 with the same spectroscopic redshift (see Section 3.1 for details).

with the latter's AGN classification relying on an X-ray luminosity just above the (constant) threshold. There is also an X-ray source in ALESS 17.1, but it appears to be associated with a companion to the 870 μm bright SMG (see Figure 1). The presence of a bright AGN could enhance the central brightness of the observed stellar distribution and lead to a higher Sérsic index; we note that this will not affect the majority of the sample.

2.2. JWST Observations and Data Reduction

The JWST data presented here are part of a GO Cycle 1 Program (PID 2516, PIs: Hodge & da Cunha) to perform near- and mid-infrared imaging of submillimeter galaxies from the J. A. Hodge et al. (2016, 2019) samples, as described above. The 13 primary targets were selected from the J. A. Hodge et al. (2016, 2019) samples such that they could be covered with four pointings with the NIRCam instrument (M. J. Rieke et al. 2023). Each field is imaged in the F200W, F356W, and F444W filters, using the "INTRAMODULEBOX" four-point dither pattern in order to cover a compact square region without gaps. Three NIRCam pointings used Module B only; the fourth used both Modules A and B, with an on-source exposure time of 30 minutes per field. The observations were executed between 2022 September and December. One observation was heavily impacted by slew artifacts due to persistence from bright stars on first execution, having been executed immediately following NIRCam observations of a very bright target; this was repeated in 2022 November.

The data were reduced and calibrated using version 1.11.3 of the `jwst` calibration pipeline (H. Bushouse et al. 2023) and context 1119 of the JWST Calibration Reference Data System (CRDS). We used the standard JWST calibration pipeline, broadly following the recipe and modifications from the CEERS survey (M. B. Bagley et al. 2023). The first pipeline stage, performing detector calibrations, was run with snowball detections enabled and a jump step detection threshold of 6σ. The $1/f$ noise striping pattern was removed using the `remstriping` algorithm,[32] before proceeding with the standard settings for the `calwebb_image2` pipeline, which returns photometrically calibrated images for each exposure. The third pipeline stage (`calwebb_image3`) was run in stages with some modifications, following M. B. Bagley et al. (2023); this includes the background subtraction, which uses a tiered source mask approach to compute and subtract a pedestal value for the sky, and adjusts the variance arrays in the background-subtracted images accordingly. The resulting photometry for the targets is consistent with expectations based on the MUSYC catalog (C. N. Cardamone et al. 2010) and will be discussed further in J. Li et al. (2025, in preparation). The point-spread function (PSF) FWHM in the F200W, F356W, and F444W filters is 0.″07, 0.″12, and 0.″14, respectively. For the redshift range [median redshift] of our targets, the F200W, F356W, and F444W filters will trace rest-frame 0.35–0.8 μm [0.5 μm], 0.6–1.4 μm [0.8 μm], and 0.8–1.8 μm [1 μm] stellar continuum emission,[33] respectively, with the F444W resolution corresponding to physical scales of $\sim$0.9–1.2 kpc for our range of target redshifts. A common pixel sampling of 0.″03 was used for all filters.

Given the requirement for precise alignment to the ALMA data, the astrometric calibration is an important aspect of the data reduction, and this calibration step proved challenging due to the lack of point sources in our fields. The `tweakreg` step was used to perform both the relative and absolute alignments, the latter using the Gaia DR3 catalog (Gaia Collaboration et al. 2023). However, some modifications were used for the individual pointings to optimize the outcome of the adjustment. These include removing Gaia sources without proper-motion information from the reference catalog[34]; and removing poorly centroided sources from the pipeline-created source catalogs and/or using PSF photometry to improve centroids, especially for partially saturated sources.

The resulting relative and absolute astrometric accuracy was estimated from the final mosaics, by comparing measured

[32] https://github.com/ceers/ceers-nircam

[33] We note that the Hα and [O III]$\lambda\lambda$ 5007,4959 emission lines may fall in the F200W or F356W filters for the redshift range of our targets (e.g., J. McKinney et al. 2023). However, given the wide filter bandwidths and relatively low equivalent width lines expected for the sources targeted here (<25 Å/<250 Å for [O III]/Hα; E. J. Birkin 2022; D. Taylor et al. 2024, in preparation), this is not expected to impact the current analysis.

[34] See https://github.com/spacetelescope/jwst/issues/8168 for a discussion of this issue.

point-source centroids between filters, and computing the average offset between the NIRCam and Gaia DR3 catalog coordinates, respectively. The resulting astrometric accuracies are shown in the Appendix. We also list the number of Gaia stars available for absolute alignment. We estimate a median absolute uncertainty in the astrometric solutions of 0.″03 (i.e., one pixel).

2.3. ALMA Data

The ALMA continuum observations utilized for the primary targets in this study were taken as part of programs 2012.1.00307.S and 2016.1.00048.S and previously presented in J. A. Hodge et al. (2016, 2019), respectively. For both studies, the frequency setup was centered at 344 GHz (Band 7; 870 μm observed frame) with 4 × 128 dual polarization channels covering the 8 GHz bandwidth in Time Division Mode (TDM). At the median redshift of our targets ($z \sim 3$), 870 μm corresponds to 210 μm in the rest frame. The naturally weighted continuum data were imaged with pixel scales of 0.″02 and 0.″01 and achieved angular resolutions of 0.″17 × 0.″15 and 0.″10 × 0.″07 for the analyses of J. A. Hodge et al. (2016) and J. A. Hodge et al. (2019), respectively (corresponding to physical scales of $\sim 1.3 \times 1.2$ kpc and $\sim 800 \times 550$ pc at a redshift of $z \sim 3$). This range of spatial resolutions is similar to that achieved by NIRCam from 2.0-4.4 μm (0.″07–0.″14). The typical rms noise achieved in the 870 μm continuum images is 64 μJy beam^{-1} (for the 0.″16 images) and 20 μJy beam^{-1} (for the 0.″08 images). As discussed in J. A. Hodge et al. (2016) and J. A. Hodge et al. (2019), the median flux density recovered from the sources in these high-resolution maps is consistent with the results from previous low-resolution observations (1.″6; J. A. Hodge et al. 2013). The two most discrepant sources (ALESS 76.1 and 112.1) have a recovered flux density that is ∼15%–20% lower than the low-resolution value, but given the large uncertainties on the latter, the flux densities still agree within 2σ. The high-resolution maps thus do not appear to be resolving out low-surface-brightness emission due to the array configuration, consistent with the maximum recoverable scales probed. Given the angular resolution of the 870 μm observations and the high signal-to-noise ratio (S/N) of the targets, the *statistical* astrometric accuracy is likely limited by the phase variations over the array to a few [10] mas for images with 0.″08 [0.″16] resolution.[35]

3. Analysis and Results

3.1. Stellar Emission Compared to Dust Continuum

Figure 1 shows 8″ × 8″ (∼65 × 65 kpc at $z \sim 3$) three-color ("RGB") images of the 13 primary targets. The RGB images were made with the NIRCam F444W (red), F356W (green), and F200W (blue) filters. The stellar counterparts to all of the SMGs are visible in the NIRCam RGB images. Interestingly, the NIRCam imaging also reveals an apparent tidal connection between ALESS 1.1 and 1.2 (which have spectroscopic redshifts of $z = 4.674$ and $z = 4.669$, respectively), providing the first direct evidence for an ongoing interaction. We note that while ALESS 1.3 also lies nearby, its photometric redshift ($z = 2.86^{+0.46}_{-1.53}$) indicates it may be at lower redshift.

Also apparent in Figure 1 is a galaxy ∼5″ south of ALESS 3.1 that was not detected at 870 μm in the original ALESS survey (J. A. Hodge et al. 2013) but was strongly detected in the subsequent much deeper (and high-resolution) follow-up ALMA imaging utilized in this work, with an integrated flux density of $S_{870} = 1.07 \pm 0.06$ mJy (this is fainter than the 3.5σ limit of the original ALESS map, which had $\sigma_{870} = 0.41$ mJy beam^{-1}; J. A. Hodge et al. 2013). ALESS 3.1-comp is only ∼40 km s^{-1} offset from ALESS 3.1 (based on a recent CO(5–4) detection; B. Westoby et al. 2025, in preparation) and has a projected nuclear separation with ALESS 3.1 of ∼ 40 kpc. Given this, its strong submillimeter emission, and the tidal features apparent in the NIRCam images (Figure 2), it is possible that this galaxy is undergoing an early-stage interaction/merger with ALESS 3.1. We therefore refer to it as "3.1-companion" (hereafter "3.1-comp") and include it in the primary sample in Table 1 and for the analysis in the remainder of the paper.

To investigate how the morphology of the sources changes with wavelength, Figure 2 shows 3″ × 3″ cutouts (∼25 × 25 kpc at $z \sim 3$) of the 13 sources in each of the NIRCam filters along with the corresponding RGB images. All of the sources are detected in at least the F356W and F444W NIRCam filters (i.e., longward of 3.5 μm observed-frame), including the red stellar counterpart to ALESS 17.1, which lies ∼0.″8 from an optically bright spiral galaxy companion at the same redshift.[36] The majority of the sources show much weaker and/or centrally suppressed emission in NIRCam's F200W filter compared to the F356W/F444W filters, highlighting the red galaxy centers. Some apparent tidal features are also visible; we indicate a few prominent examples in Figure 2 in the filter where they are most evident.

Figure 3 shows a comparison of the JWST NIRCam RGB imaging (zoomed to 2″ × 2″) and the high-resolution 870 μm imaging for the 13 sources. The morphologies of the (typically) rest-frame near-infrared stellar and dust continuum images (traced by F444W and 870 μm, respectively) show some striking similarities (as well as some notable differences), which we explore further below. Here, we note that the peak of the emission from the rest-frame near-infrared counterpart (measured from the peak pixel in the F444W filter) is consistent with the peak of the 870 μm emission to within the F444W PSF FWHM of < 0.″14 (∼1 kpc) for the majority (9/13) of the galaxies: ALESS 3.1, 3.1-comp, 9.1, 10.1, 15.1, 17.1, 29.1, 45.1, and 112.1. For the remaining four sources (ALESS 1.1, 1.2, 1.3, and 76.1), the peak of the 870 μm emission is ⩾0.″14 from the peak of the apparent counterpart in the F444W imaging, with the largest offset measuring 3 kpc (for ALESS 1.3, where the 870 μm emission may be more consistent with the fainter of what appear to be two marginally blended components in the NIRCam images). For the sources with significant offsets, this may indicate either that the ALMA 870 μm and NIRCam imaging are tracing physically distinct components in these sources, or that the detected stellar emission traced by the NIRCam F444W filter is still experiencing significant dust attenuation. We explore these possibilities further below.

[35] ALMA Cycle 11 Technical Handbook, Chapter 10.5.2.

[36] SINFONI spectroscopic imaging previously indicated that the two galaxies lie at the same redshift (C.-C. Chen et al. 2020); this is further confirmed by recent high-resolution ALMA CO(5–4) imaging (B. Westoby et al. 2025, in preparation)

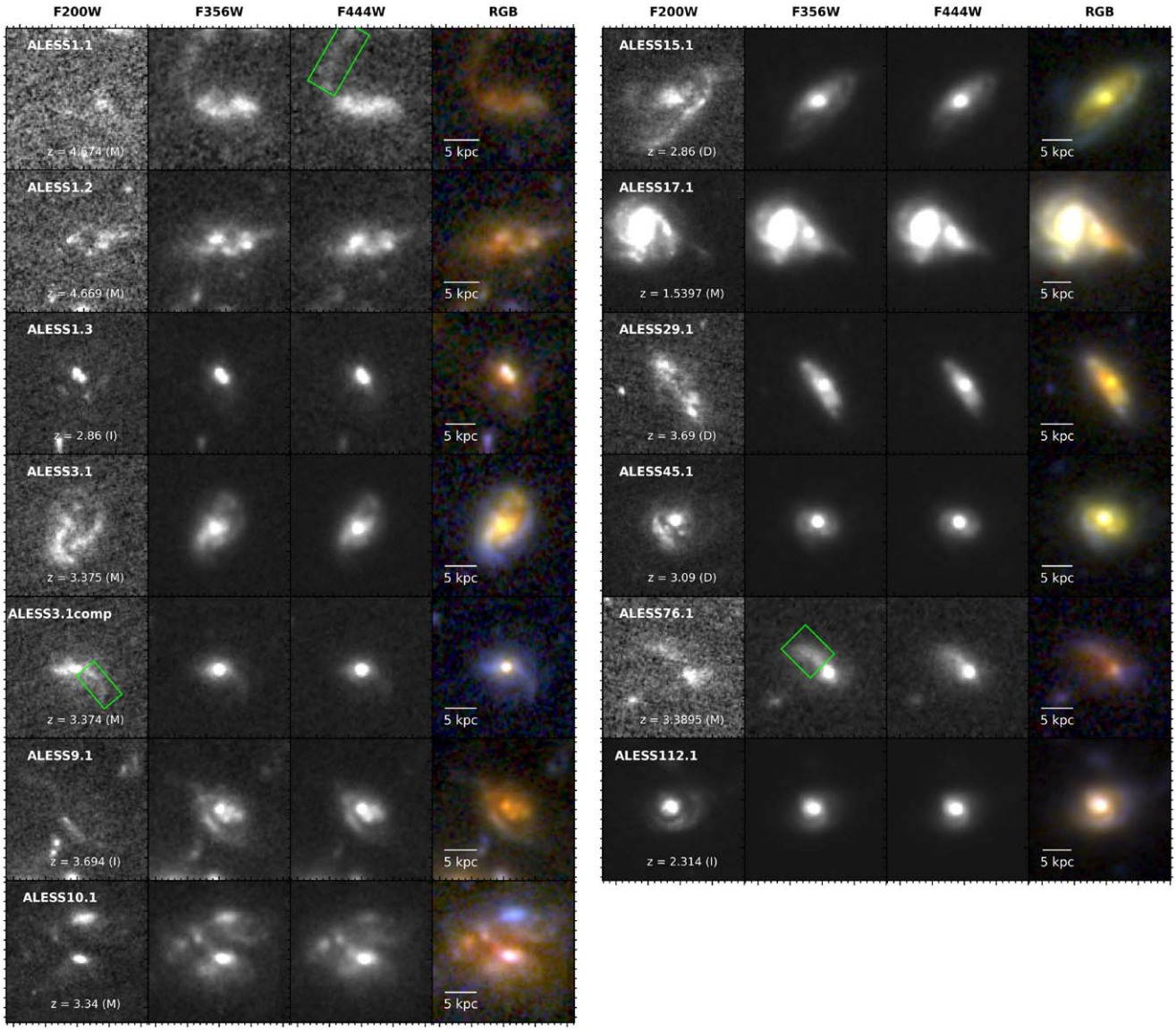

Figure 2. JWST NIRCam cutouts ($3'' \times 3''$, or $\sim 25 \times 25$ kpc at $z \sim 3$) of the 13 sources. For each galaxy, the columns show (from left): F200W, F356W, F444W, and the corresponding RGB image. Individual filters are scaled with a linear stretch between 0.25% and 99.5%, except for ALESS 17.1, where a maximum of 95.0% is used to highlight the faint red submillimeter galaxy to the west and the brighter companion to the east. Most of the targeted SMGs are heavily dust-attenuated even with NIRCam's 2 μm filter but are significantly less obscured above 3.5 μm ($\simeq$1 μm rest-frame). Some examples of apparent tidal tails are highlighted with boxes in the filter where they are most visible, and the panels are labeled with redshift and visual classification (disk, indeterminate, or merger; see Section 3.2.)

3.2. Visual Classification

We next visually classify the galaxies into three broad classes:

(M) "Merger": Sources with evidence for a merger or interaction;
(I) "Indeterminate";
(D) "Disk": Sources with no clear evidence for a merger or interaction, and which thus appear as undisturbed disks.

To determine the visual classification for each galaxy, five coauthors independently classified the morphology of each of the 13 sources, taking into account the rest-frame near-infrared and 870 μm morphologies (and further informed by the presence of a companion at the same redshift, if applicable). For each galaxy, we adopt the modal classification (preferred by at least 3/5 classifiers; three-fifths); if no majority classification resulted from this method, then the galaxy was automatically assigned class I (indeterminate). We then calculated the fraction of sources in each of the three classes. Given the subjective nature of such classifications, we take the difference between the fraction in a given class (i.e., from the above method) and the fraction from the most discrepant individual classification (i.e., by any one classifier) and adopt it as a rough estimate of the uncertainty.

With the above method, we find the following results: M: 54% $\pm$ 23% (show evidence of mergers); I: 23% $\pm$ 31% (indeterminate); D: 23% $\pm$ 8% (appear as undisturbed disks). These results indicate that the majority of the galaxies in the current sample show signs of ongoing major/minor mergers or interactions, while only a minority show no clear evidence from the current data sets. Larger samples of galaxies spanning a wider range of 870 μm flux density (e.g., S. Gillman et al. 2024) will be required to determine the importance of mergers/interactions for the SMG population as a whole.

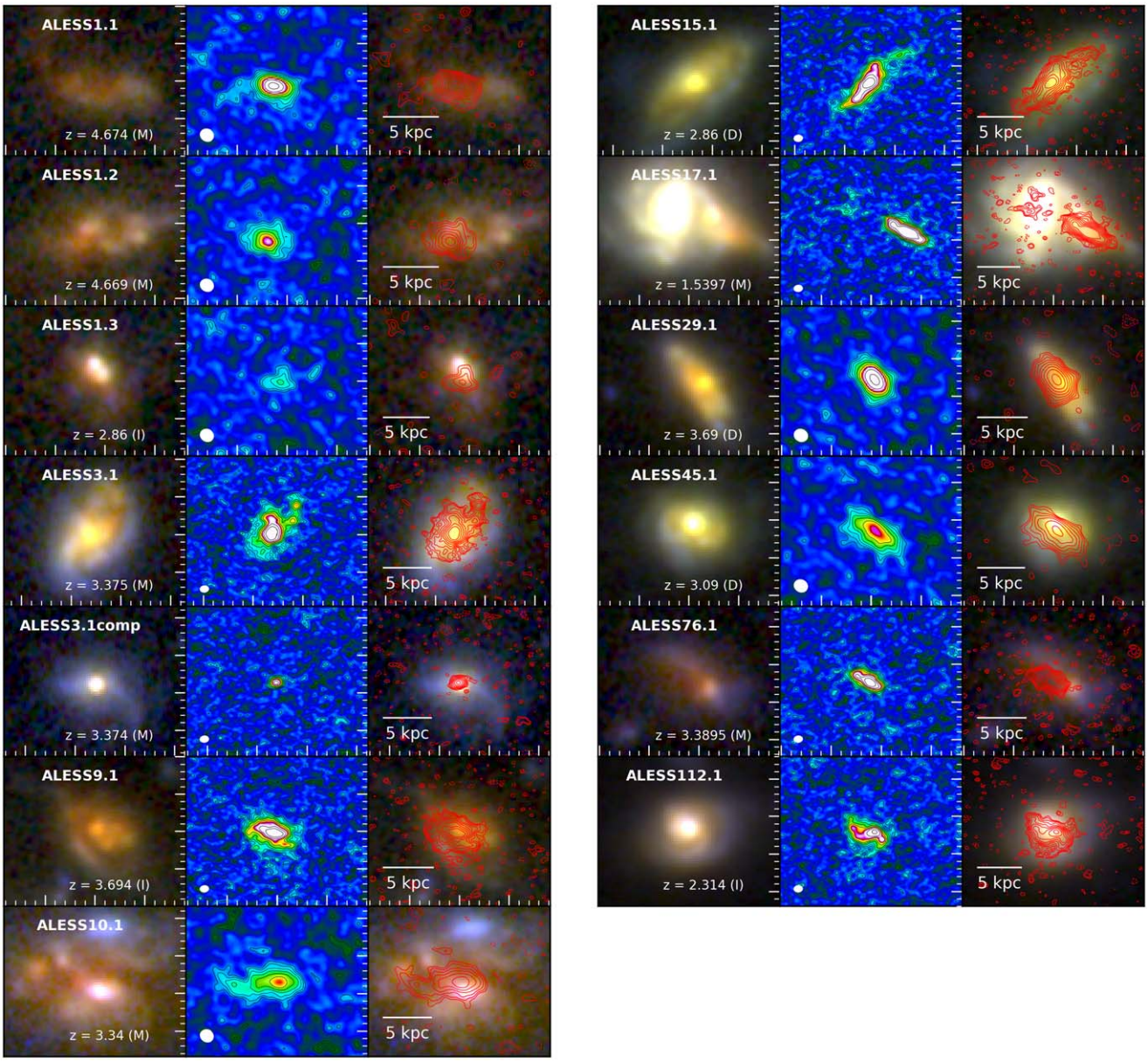

Figure 3. JWST NIRCam vs. ALMA 870 μm imaging for the 13 SMGs. For each source, the columns show the NIRCam RGB image (constructed from F444W, F356W, and F200W; left), the ALMA 870 μm image (middle), and the ALMA contours in red overlaid on the RGB image (right). The ALMA images are scaled with a power-law stretch between -10σ and 20σ (exponent $= 2.1$), with ALMA contours starting at 2σ (or -2σ for negative contours) and increasing in powers of $\sqrt{2}$. Panels are $2'' \times 2''$, or $\sim$15 kpc at $z \sim 3$. The NIRCam images reveal the rest-frame near-infrared morphologies of the galaxies on the same (sub)kiloparsec scales as the 870 μm dust continuum, with the 870 μm emission tracing the dust-reddened centers as well as some more extended features.

3.3. Flux Density Profiles

To determine the effective radii of the galaxies in each filter, we create curves of growth. We first run SEXTRACTOR (E. Bertin & S. Arnouts 1996) on the NIRCam images with a detection threshold of 3.0 times the local noise, a minimum number of pixels above the threshold of 12 at $0\farcs03$ sampling per pixel, and DEBLEND_MINCONT set to 0.05. The latter parameter prevents deblending ALESS1.2 and ALESS10.1 into two sources each. We determine the aperture shape for each source using the results from the F444W filter (chosen to minimize extinction), with the centroid taken as the peak pixel in 870 μm, which will be more robust against dust-obscuration effects than the NIRCam filters. We then use PHOTUTILS (L. Bradley et al. 2022) to measure the flux density in elliptical apertures as a function of distance along the major axis, with the total integrated flux density in each filter taken using the F444W maximum aperture (again, to minimize extinction effects, and after ensuring the emission from all filters is covered). Finally, we use the same apertures to measure the flux density in the 870 μm image for each source.

Figure 4 shows the effective radii (and median values) derived from this method versus observed wavelength, and including both the NIRCam and 870 μm measurements. Here we exclude ALESS 17.1 due to confusion with its optically bright companion in the JWST images. The values for individual sources can be found in Table 2, and the flux density profiles themselves can be found in the Appendix.

We find that the effective radius measured for the galaxies systematically decreases with increasing wavelength for the majority of the sources, with median values (and bootstrapped

Table 2
Morphology with JWST and ALMA

Source ID	NIRCam F444W				ALMA 870 μm				Classification[c]
	n[a]	b/a[a]	PA[a] (deg)	R_e[b] (kpc)	n[a]	b/a[a]	PA[a] (deg)	R_e[b] (kpc)	
ALESS 1.1	0.36 ± 0.04	0.37 ± 0.07	85 ± 13	$4.2^{+0.4}_{-0.4}$	1.6 ± 0.2	0.45 ± 0.05	80 ± 8	$2.1^{+0.2}_{-0.1}$	M
ALESS 1.2	0.59 ± 0.06	0.38 ± 0.07	98 ± 15	$4.2^{+0.3}_{-0.3}$	2.5 ± 0.3	0.75 ± 0.10	80 ± 9	$2.5^{+0.4}_{-0.2}$	M
ALESS 1.3	1.8 ± 0.2	0.5 ± 0.1	36 ± 5	$2.5^{+0.3}_{-0.2}$	1.5 ± 0.2	0.45 ± 0.05	102 ± 8	$1.9^{+1.0}_{-0.4}$	I
ALESS 3.1	1.1 ± 0.1	0.6 ± 0.1	142 ± 21	$3.1^{+0.2}_{-0.1}$	1.4 ± 0.1	0.67 ± 0.07	139 ± 4	$1.82^{+0.08}_{-0.08}$	M
ALESS 9.1	1.2 ± 0.1	0.7 ± 0.1	62 ± 9	$2.8^{+0.2}_{-0.1}$	0.68 ± 0.07	0.54 ± 0.05	72 ± 7	$1.50^{+0.05}_{-0.07}$	I
ALESS 10.1	1.2 ± 0.1	0.8 ± 0.1	80 ± 12	$5.3^{+0.2}_{-0.2}$	1.0 ± 0.1	0.33 ± 0.03	93 ± 9	$1.8^{+0.3}_{-0.2}$	M
ALESS 15.1	1.6 ± 0.2	0.47 ± 0.08	127 ± 19	$3.8^{+0.1}_{-0.1}$	0.87 ± 0.08	0.36 ± 0.04	138 ± 4	$2.14^{+0.07}_{-0.07}$	D
ALESS 17.1[d]	0.54 ± 0.05	0.6 ± 0.1	48 ± 9	—	0.54 ± 0.05	0.27 ± 0.03	62 ± 6	—	M
ALESS 29.1	0.89 ± 0.09	0.37 ± 0.07	34 ± 5	$3.0^{+0.1}_{-0.1}$	0.68 ± 0.07	0.55 ± 0.06	34 ± 3	$1.42^{+0.10}_{-0.07}$	D
ALESS 45.1	1.8 ± 0.2	0.8 ± 0.2	70 ± 11	$2.4^{+0.1}_{-0.1}$	0.48 ± 0.05	0.40 ± 0.04	54 ± 6	$1.8^{+0.2}_{-0.1}$	D
ALESS 76.1	1.6 ± 0.2	0.5 ± 0.1	51 ± 8	$3.2^{+0.3}_{-0.2}$	0.62 ± 0.06	0.50 ± 0.05	63 ± 6	$1.24^{+0.07}_{-0.07}$	M
ALESS 112.1	1.5 ± 0.1	1.0 ± 0.2	73 ± 16	$2.6^{+0.1}_{-0.1}$	0.48 ± 0.05	0.54 ± 0.05	70 ± 7	$1.81^{+0.12}_{-0.09}$	I
ALESS 3.1-comp	5.4 ± 0.5	0.7 ± 0.1	89 ± 14	$2.0^{+0.3}_{-0.2}$	1.1 ± 0.2	0.87 ± 0.14	148 ± 13	$0.53^{+0.22}_{-0.09}$	M

Notes.
[a] Derived from Sérsic fitting using GALFIT (Section 3.4).
[b] Derived from flux density profiles with PHOTUTILS (Section 3.3).
[c] Classifications are: (M) sources with evidence for a merger/interaction; (I) indeterminate; and (D) sources with no clear evidence for a merger/interaction, and which thus appear as undisturbed disks. See Section 3.2 for further details.
[d] The parameters reported here are for the SMG, not the optically bright companion.

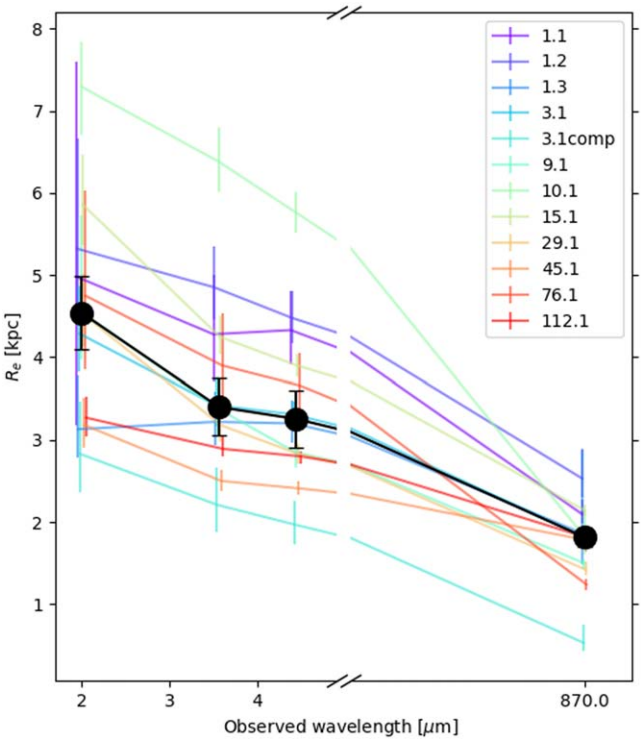

Figure 4. Effective radius vs. wavelength for the sources (excluding 17.1 due to confusion with its optically bright companion). Individual sources are shown in different colors. The sample median is shown with the large black circles, where the error bars were calculated using bootstrapping. Including both the NIRCam and 870 μm observations, we find that the median effective radius systematically decreases with increasing wavelength.

errors) of 0.″61 ± 0.″08, 0.″45 ± 0.″06, and 0.″41± 0.″05 for the F200W, F356W, and F444W filters, respectively. These values correspond to 4.5 ± 0.5 kpc, 3.4 ± 0.4 kpc, and 3.0 ± 0.3 kpc using the individual source redshifts, with 16th–84th percentile ranges of 3.0–5.3 kpc (F200W), 2.4–4.4 kpc (F356W), and 2.4–4.2 kpc (F444W). The effective radius then decreases even further for the majority of the sources at 870 μm, with a median value of 0.″23 ± 0.″01 (1.8 ± 0.1 kpc, with a 16th–84th percentile range of 1.4–2.1 kpc). Overall, the median effective radius of the galaxies at F200W [F356W] is 48% ± 30% [10% ± 20%] larger than that measured at F444W, reflecting the relative brightness of the red galaxy centers at the reddest wavelengths. We explore whether this trend is due to dust obscuration in the following Sections. Meanwhile, the median effective radius at F444W is 78% ± 21% larger than that measured with ALMA at 870 μm. We note that if we had instead used the peak F444W pixel positions as the aperture centers, our conclusions would not change. We thus find a much more compact dust continuum than rest-frame ∼1 μm light, consistent with earlier indications from select sources (e.g., C.-C. Chen et al. 2022; S. Gillman et al. 2024).

3.4. GALFIT Modeling

To compare the morphology of the NIRCam-detected stellar emission with that of the 870 μm dust continuum in more detail, we fit both the F444W images (chosen to minimize dust extinction) and the 870 μm images with single 2D Sérsic profiles using GALFIT (C. Y. Peng et al. 2002, 2010). We consider only single-component profiles for a more straightforward comparison between parameters. For the 870 μm image fitting, we use the ∼0.″16 870 μm ALMA maps available for all of our targeted galaxies and the procedure outlined in J. A. Hodge et al. (2016). We verify that we recover the results of J. A. Hodge et al. (2016), noting that J. A. Hodge et al. (2019) found Sérsic indices that agreed within the errors for sources also observed at the higher resolution (0.″08) with ALMA.

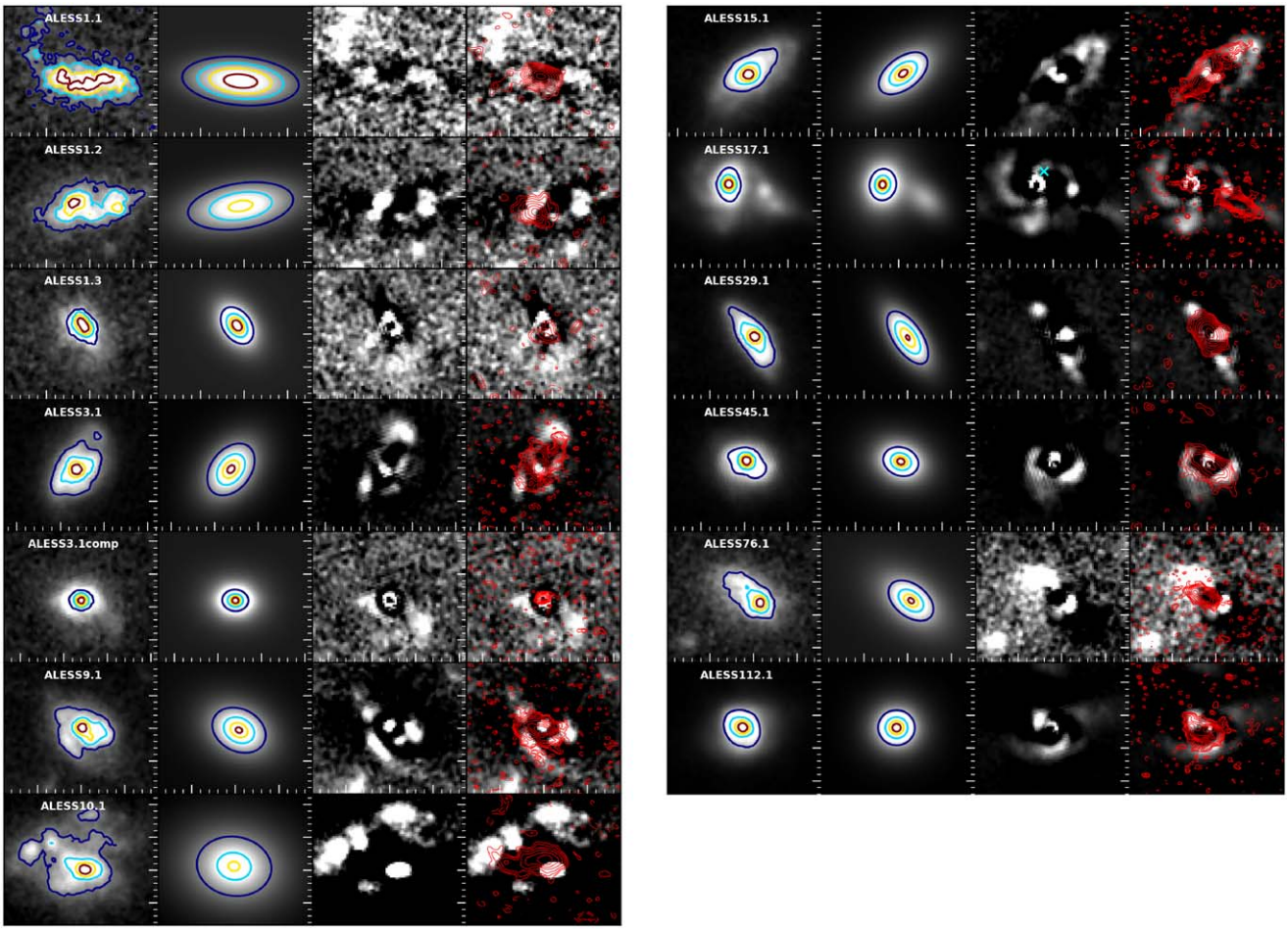

Figure 5. GALFIT modeling of the NIRCam F444W images for the 13 targeted SMGs. For each source, the columns show the NIRCam F444W image (first column), the best-fit Sérsic profile model (second column), the residuals (third column), as well as a comparison of those residuals to the ALMA 870 μm contours overlaid in red (fourth column). The first and second columns are scaled with a linear stretch between 0.25% and 99%, with contours showing 20%, 40%, 60%, and 80% of the peak intensity of the data (i.e., column 1). The third and fourth columns are shown with a linear stretch and the peak intensity scaled down by a factor of 5 to highlight the discrepancies. We note there is no qualitative difference to the residuals when the fits with freely varying n-values are shown instead. 870 μm contours start at 2σ (or -2σ for negative contours) and increase in powers of $\sqrt{2}$, where $\sigma = 19$ μJy. Panels are $2'' \times 2''$, or ~ 15 kpc at $z \sim 3$. See Section 3.4 for details. The cyan cross overlaid on the third column for ALESS 17.1 shows the position of the known X-ray active galactic nucleus (AGN; corrected for the median offset between the X-ray catalog and Gaia DR1; B. Luo et al. 2017), indicating it is associated with the optically bright companion rather than the SMG.

For the fitting of the F444W images, we obtain the most realistic PSFs by adopting the following strategy: We first use WEBBPSF v1.2.1 (M. D. Perrin et al. 2014) to generate the F444W PSF oversampled by a factor of 4. We then match the simulated PSF to our science data for each target using the `webbpsf.setup_sim_to_match_data` utility. Finally, to further improve these models, we follow C.-C. Chen et al. (2022) and use GALFIT to convolve the resulting PSFs with Gaussian profiles and fit them to nearby (unsaturated) stars. This results in reduced χ^2 values of $\sim$1, and we therefore adopt the best-fit (normalized) models as the final PSFs. We then run GALFIT, masking the other sources in the field using the segmentation maps from SEXTRACTOR (and with the parameters presented in Section 3.3). For initial parameter guesses, we use the parameters derived from the 870 μm image fitting, but we checked that our results were not sensitive to the exact input parameters. For ALESS 17.1, we simultaneously fit the SMG and its optically bright companion.

Figure 5 shows the results of running GALFIT on the F444W images (where the values of the resultant Sérsic indices, axis ratios, and position angles can be found in Table 2). From the residual panels, it is evident that many sources contain structures beyond a single Sérsic profile. For example, roughly half of the sources (ALESS 3.1, 3.1-comp, 9.1, 15.1, 29.1, and 45.1) show evidence for excess emission beyond the models that is concentrated near the galaxy centers. A comparison of the GALFIT residuals with the high-resolution 870 μm imaging shows that this excess emission is aligned with the peak of the 870 μm emission in the majority of the cases. These central residuals are thus potentially evidence for bulge-like components and/or bright central AGNs, as also reported in JWST imaging studies of submillimeter-fainter sources (e.g., C.-C. Chen et al. 2022). As ALESS 45.1 is currently the only SMG in the sample that may host an AGN, bulge-like components may be the more likely explanation for the majority of the sources.

Beyond these central stellar concentrations, there are additional residual structures evident in Figure 5 that are not captured in the GALFIT models. In particular, we see excess emission in the outskirts of several of the sources, further highlighting some of the features already apparent in Figure 2 resembling tidal tails/plumes (e.g., see ALESS 3.1 and 3.1-comp). Interestingly, some of these potential tidal features are also partially detected in the 870 μm continuum (see Figure 5)

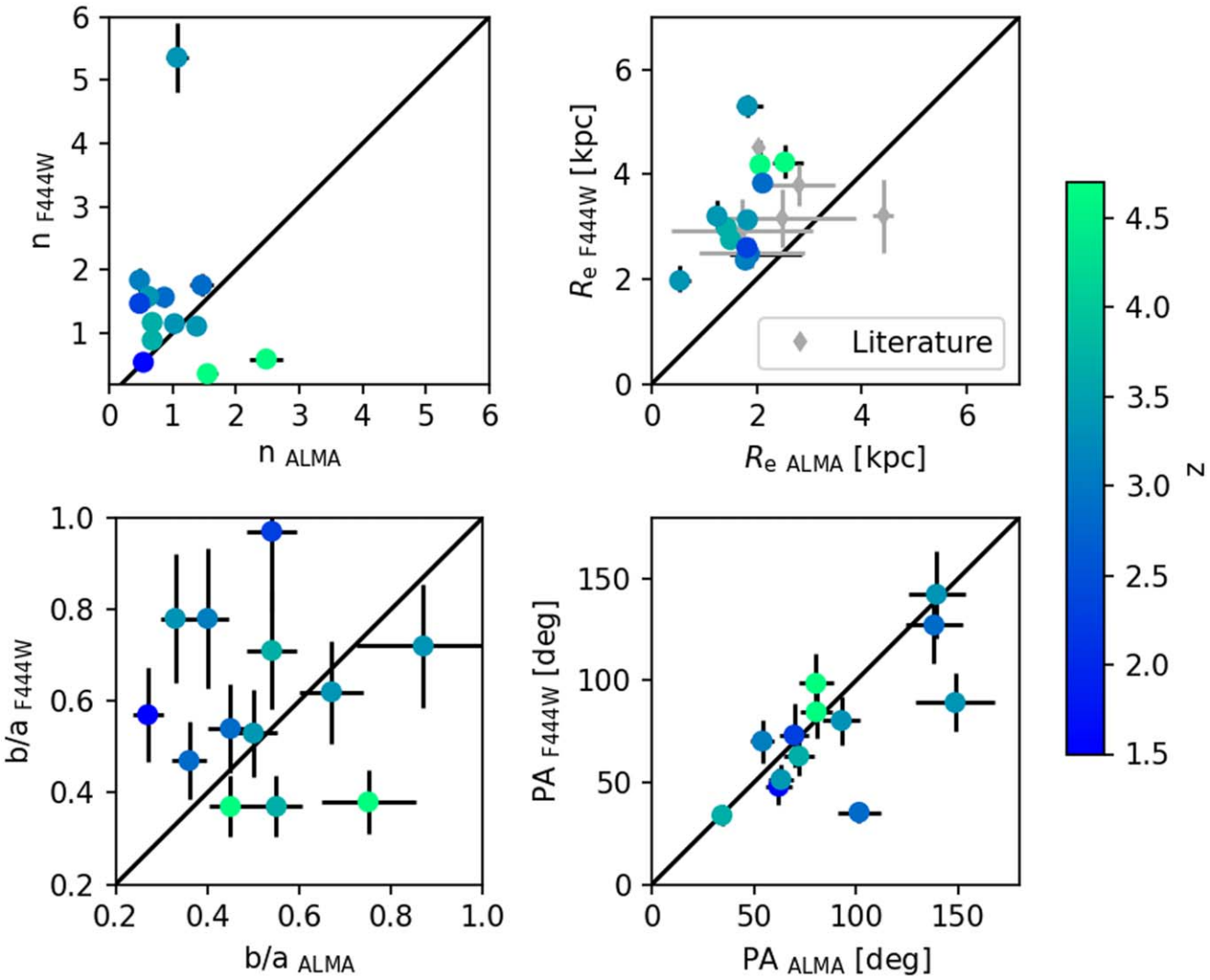

Figure 6. Comparison of the morphological parameters derived from the F444W images with those from the 870 μm images. The panels showing the Sérsic index n (upper left), the axis ratio b/a (bottom left), and the major axis position angle (PA, bottom right) were derived using GALFIT with single Sérsic profile fits (Section 3.4). For the axis ratio and position angle, the Sérsic index is fixed to $n = 1$ to facilitate direct comparison. The effective radii R_e (upper right) were derived nonparametrically using curves of growth (Section 3.3). All data points are color-coded by redshift. The literature SMGs in the top-right panel show other sources with measurements at both wavelengths (compiled from C.-C. Chen et al. 2022; C. Cheng et al. 2023; P. S. Kamieneski et al. 2023; I. Smail et al. 2023). Comparing the F444W- and 870 μm-derived parameters, we find a strong positive correlation along the one-to-one line between the position angles, a tentative positive correlation between the effective radii, and no correlation between either the Sérsic indices or axis ratios.

for the sources with the highest-resolution 870 μm imaging (e.g., ALESS 3.1, 9.1, and 112.1, though we note that the classification of these features can be somewhat subjective; Section 3.2).

Figure 6 shows a comparison of the morphological parameters derived for each galaxy from the F444W and 870 μm images. (The optically bright companion to ALESS 17.1 is not included in this plot due to its low S/N in the 870 μm image; see Figure 3.) The Sérsic index (n), ellipticity (b/a), and position angle (PA) were taken from the best-fit GALFIT models. As the uncertainties reported by GALFIT are well known to be unrealistically small (A. van der Wel et al. 2012; A van der Wel et al. 2024), we generate more realistic error bars by comparing to the results from STATMORPH (V. Rodriguez-Gomez et al. 2019), which allows for both parametric (Sérsic) and nonparametric fitting. For the Sérsic index, the median ratio of the values returned by the two codes is 1.0 with a 16th–84th percentile range of 0.91–1.03 (i.e., $1\sigma \simeq 6\%$ for a normal distribution), and we therefore conservatively include a 10% fractional uncertainty in quadrature on our reported error bar. For the PA and b/a, a similar comparison with the results from the STATMORPH Sérsic fit reveals fractional uncertainties of a $\sim$few percent, while a comparison with the nonparametric estimates suggests fractional uncertainties of $\sim$15% (PA) and $\sim$18% (b/a). We therefore conservatively take the latter (higher) values and add them in quadrature to the uncertainties on those parameters. We note that we also find a $\sim$20% *systematic* offset between the b/a values measured from the Sérsic and nonparametric fits (in the sense of more circular profiles according to the nonparametric fitting). However, this is not necessarily surprising given the fundamentally different nature of the profiles being fitted, and we explore any potential impact on our results below. Finally, we fix the Sérsic indices n to 1.0 for both F444W and 870 μm to ensure a more straightforward comparison when fitting the other relevant structural parameters (b/a and PA).

We take the difference between the parameters calculated with n held fixed and allowed to vary and add this in quadrature as an additional systematic uncertainty for these parameters.

Figure 6 also shows a comparison of the best-fit effective radii (R_e) measured in the 870 μm and F444W images using the curve of growth analysis of Section 3.3. For the F444W images, the R_e values derived from GALFIT are consistent with the curve-of-growth values within the uncertainties. For the 870 μm images, the two methods also produce consistent results for all sources except ALESS 1.1, where GALFIT prefers (at $>3\sigma$) a smaller radius (0.9 ± 0.1 kpc). Given that the (nonparametric) curve of growth analysis is less sensitive to morphological asymmetries, we consider these values the fiducial values. However, we note that if we instead used the GALFIT-derived results, it would only strengthen our finding that the dust continuum is more compact than the rest-frame $\sim$1 μm (Section 3.3).

From Figure 6, we see that some of the morphological parameters describing the dust continuum and detected stellar distributions are more tightly correlated than others. To quantify this effect, we calculate the Pearson correlation coefficient, ρ, between the F444W- and 870 μm-derived parameters, which measures the strength of the linear monotonic correlation between two sets of data.[37] We find values of ρ (and corresponding probabilities) of -0.14 (0.65), $+0.68$ (0.01), -0.02 (0.94), and $+0.72$ (0.005) for n, R_e, b/a, and PA, respectively.[38]

This exercise indicates that the position angle is the morphological parameter that shows the strongest correlation (of those tested) between the F444W and 870 μm images. Moreover, as Figure 6 shows, the position angle is not just strongly correlated, but it is correlated along the one-to-one line. This result indicates that the global morphologies of the rest-frame infrared and dust continuum emission are generally well-aligned. This close agreement can be attributed to the fact that the deep 870 μm imaging—while more compact than the F444W emission for these galaxies—nevertheless still traces rest-frame near-infrared structures beyond the central bulges (/bars). In particular, the global PA agreement seen here appears to be driven in at least some cases by the (apparent) tidal features detected in the outskirts of some sources in both the 870 μm emission as well as in the detected stellar emission (e.g., Figure 3). Meanwhile, the two clear outliers from the PA comparison in Figure 6 are both understandable: ALESS 1.3 shows evidence for two marginally blended components in the NIRCam imaging (driving the PA), and the 870 μm image of ALESS 3.1-comp is relatively shallow and compact compared to NIRCam.

In addition to the strong correlation of the position angles, the effective radii show a tentative positive correlation. However, we also find—perhaps surprisingly—that the axis ratios show no correlation. As mentioned above, if we measure the axis ratios in the F444W maps using a nonparametric method instead, we find values that are systematically $\sim$20% higher than those from the Sérsic fits, indicating more circular light profiles. However, if we use those values and recalculate the strength of the correlation with the 870 μm traced structures, the lack of correlation persists (Pearson's $\rho = +0.06$ and corresponding probability of 0.84). This lack of correlation may be due to a real physical difference in the gas and stellar distributions, dust obscuration, or the fact that the axis ratios are tracing structure at smaller radii in the 870 μm emission.

We also find no correlation between Sérsic indices in the F444W and 870 μm emission. The Pearson's correlation coefficient suggests a mild anticorrelation, which may be caused by the influence of central dust obscuration on the F444W profiles, but it is not statistically significant. We note that the most extreme outlier from this plot, ALESS 3.1-comp, shows a very high Sérsic index in the F444W image ($n = 5.4 \pm 0.5$), which may hint at the presence of a bright compact nucleus (either a star cluster or a type 1 AGN) in the center.

3.5. Isophotal Fitting: Searching for Stellar Bars

Given the previous evidence for bar-like features in the dust continuum in SMG samples (e.g., B. Gullberg et al. 2019), and in particular, the elongated central features visible in the high-resolution images of some of the current targets (J. A. Hodge et al. 2019), one might expect to find evidence for stellar bars. We thus search for potential stellar bars in the sources by fitting elliptical isophotes to the F444W images using PHOTUTILS. Using this method, the surface brightness, ellipticity ($e = 1 - b/a$), and position angle of the fitted ellipses are allowed to vary as a function of distance along the semimajor axis, which increases by a factor of 1.1 for each subsequent ellipse fit. The fitting continues until either the relative error in the local radial intensity gradient is >0.5 for two consecutive ellipse fits or the outermost ellipse extends to the low signal-to-noise region ($S/N \leqslant 3$). For comparison, we fit the highest-resolution 870 μm data available for each galaxy.

Following Y. Guo et al. (2023), we carry out the ellipse fitting in a two-step process: (1) In the first iteration, we keep the center of each fitted ellipse as a free parameter. (2) In the second iteration, we fix the center of all ellipses to the mean center found from fitting the inner six ellipses (i.e., central $0\farcs3$) in step 1.

To ensure that any bars identified are reliable, we exclude highly inclined sources (with $i > 60$ deg as inferred from the projected axis ratios of the outermost ellipse in F444W). This excludes only ALESS 1.1 and ALESS 1.2. We exclude also ALESS 17.1 due to confusion with its companion but include all 10 remaining sources, including those that are clearly clumpy as a test of the robustness of the methodology.

We then test whether the resulting radial profiles meet the following criteria, which are characteristic of stellar bars (e.g., H. Wozniak et al. 1995; S. Jogee et al. 2004; I. Marinova & S. Jogee 2007):

1. The ellipticity (e) rises smoothly to a global maximum $e_{max} > 0.4$ (where the position of the maximum then defines the bar end) before decreasing again in the outer disk.
2. The position angle remains fairly constant (ΔPA < 20 deg) along the bar.
3. In the transition region between the bar and outer disk, e drops by > 0.1.
4. The position angle changes by >10 deg beyond the bar end.

[37] We note that the PA is a cyclical quantity. However, as (1) we have unwrapped the PA values, and (2) the two PAs are not dictated by random processes, a linear correlation coefficient is sufficient.

[38] We note that we have also calculated the Spearman's correlation coefficients, finding values of ρ (and corresponding probabilities) of -0.28 (0.36), 0.65 (0.02), -0.09 (0.76), and 0.69 (0.009) for n, R_e, b/a, and PA, respectively. The use of the Spearman's correlation coefficients instead thus does not change our conclusions.

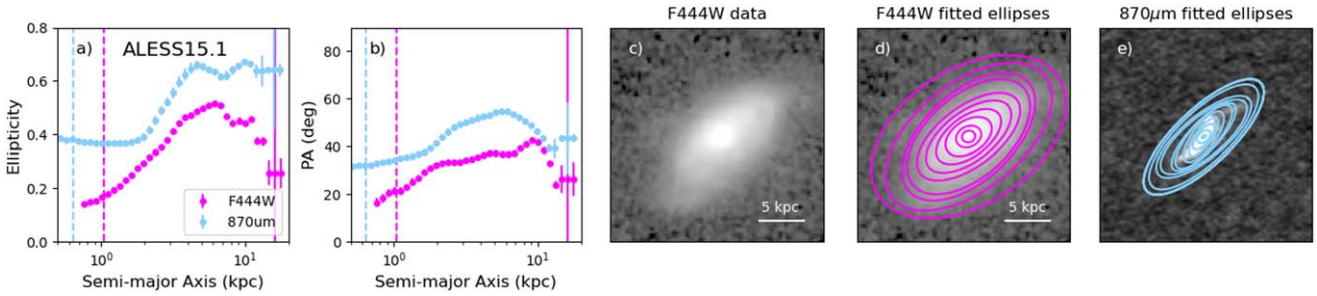

Figure 7. An example of the ellipse fitting in the F444W filter to ALESS 15.1. Panels (a) and (b) show the ellipticity and PA, respectively, in F444W of the best-fit elliptical isophotes as a function of semimajor axis. The vertical dashed lines show the scale of the respective PSFs. (Note that the errors on the fits for the second-to-last ring extend beyond the ranges plotted.) The F444W data is shown in panel (c) with log scaling, while a linear selection of best-fit isophotes are overplotted in panel (d). Panel (e) shows the best-fit elliptical isophotes for the 870 μm data for comparison. ALESS 15.1 is the only (non-clumpy) galaxy that meets all of the criteria for hosting a rest-frame near-infrared bar in the F444W imaging (see Section 3.5), but we consider this a tentative classification due to the combination of the long bar length implied, the marginally significant rotation of the PA in the outer disk, lack of evidence in the GALFIT residuals, and lack of PA correspondence between F444W and 870 μm in the inner "bar" region. We therefore find no evidence for strong rest-frame near-infrared bars in the targeted galaxies.

We note that our choice of $e_{\rm max} > 0.4$ conservatively restricts the selection to strong bars, as most (>70%) bars in near-infrared images of local spiral galaxies have ellipticities >0.4 (e.g., I. Marinova & S. Jogee 2007; K. Menéndez-Delmestre 2007) and S. Jogee et al. (2004) found that it is difficult to unambiguously identify weaker bars at $z > 1$ (but see K. Sheth et al. 2008). See Figure 1 in S. Jogee et al. (2004) for an example of radial profiles for a $z \sim 0.5$ galaxy displaying these characteristic bar signatures.

We find that no meaningful fit is possible for ALESS 10.1, which appears very clumpy/complex. The ellipse fitting also fails on the first or second iterations for ALESS 76.1 and 112.1 due to a strong dependence on the definition of the galaxy center. Given that these sources appear irregular (see the residuals from the GALFIT fitting in Figure 5), they will not be discussed further.

Out of the remaining seven galaxies, only two sources meet all of the above criteria: ALESS 9.1 and ALESS 15.1. ALESS 9.1 is clearly clumpy, so we disregard it in the remaining discussion, except as a cautionary example that the criteria above are necessary, but not sufficient, to identify bars, particularly in sources with irregular morphologies. Indeed, we also find that the apparent tidal features in the outskirts of some sources (e.g., ALESS 3.1) can cause a second peak in the ellipticity at large radii, which can complicate bar identification using the above criteria, but we have verified that we do not find any additional bar candidates if we define the "outer disk" using isophotes at smaller radii.

ALESS 15.1 is thus the only remaining bar candidate. The ellipse fitting results for this source are shown in Figure 7. If there is a bar in this source, the ellipse fitting suggests it has a maximum ellipticity of $\sim$0.5 and a semimajor axis length of $\sim$ 6.3 kpc. The latter value is within the range of bar lengths reported for $z < 1$ galaxies (e.g., S. Jogee et al. 2004), but on the large end of the range of values found for bars recently reported in $z > 1$ galaxies with JWST ($\sim$2.0–7.5 kpc; Y. Guo et al. 2023; I. Smail et al. 2023; S. Huang et al. 2023). Given (1) that this galaxy is at higher redshift ($z_{\rm phot} = 2.67$) than all but one of those sources, where bar lengths should be shorter on average due to bar size evolution (e.g., V. P. Debattista & J. A. Sellwood 2000; I. Martinez-Valpuesta et al. 2006; D. G. Algorry et al. 2017), (2) the marginal change in position angle beyond the "bar" end ($\sim$10 deg; i.e., barely above the threshold for a bar classification), (3) the lack of evidence for a bar in the GALFIT residuals, and (4) the lack of correspondence between the position angle of the F444W and 870 μm isophotes in the "bar" region (Figure 7), where we would expect agreement between the two tracers in the case of a real bar, we consider this bar classification tentative at best. We therefore find no convincing evidence for strong stellar bars in the current rest-frame near-infrared data.

3.6. NIRCam Color–Color Diagrams versus ALMA 870 μm

Lastly, we quantitatively study the relationship between the 870 μm dust continuum and detected stellar emission on $\lesssim$ 1 kpc scales to relate the influence of the former on the latter and the effect that dust obscuration has on our understanding of high-redshift star-forming galaxies. The methodology we utilize will be discussed further in J. Li et al. (2025, in preparation). In short, we first resample the 870 μm images to match the coarser NIRCam pixel scale. We use a 1000 × 1000 pixel grid with 30 mas pixels, fixing the coordinates of the target (Table 1) at the center of the central pixel. We then PSF-match the pixel-aligned NIRCam F200W, F356W and ALMA 870 μm images to the F444W filter images using PSF models from WEBBPSF and 2D elliptical Gaussians for the NIRCam PSF and ALMA synthesized beam, respectively.[39] In particular, we generated a PSF-matching kernel for each image that requires convolution using the create_matching_kernel function in the PHOTUTILS package. We then convolve these images with the PSF-matching kernel using the convolve function in the ASTROPY package after masking all other detected sources in the field of our targets.

To create color–color diagrams, we adopt an aperture grid with apertures of 2 × 2 pixels (60 mas, as these are Nyquist sampled). The fluxes within each aperture (i.e., resolution element) are summed and recorded in a table for all filters. The error on each measured flux density value was obtained by randomly placing 2 × 2 pixel apertures in the unmasked background region in the images. For apertures with $\geqslant 3\sigma$ detections in all three NIRCam filters, we compute the F200W–F356W and F356W–F444W colors and plot them in Figure 8. The data points are color-coded by their corresponding 870 μm flux density if the aperture has at least a 1σ flux density in the

[39] We note that while the ALMA resolution is nominally slightly worse than that at F444W for 6/13 sources (0.″16 versus 0.″14), the PSFs have very different shapes. In particular, the F444W PSF has a more compact core but a much more extended diffraction pattern. We thus PSF-match to F444W for all sources, noting that the exact choice of kernel does not affect our conclusions.

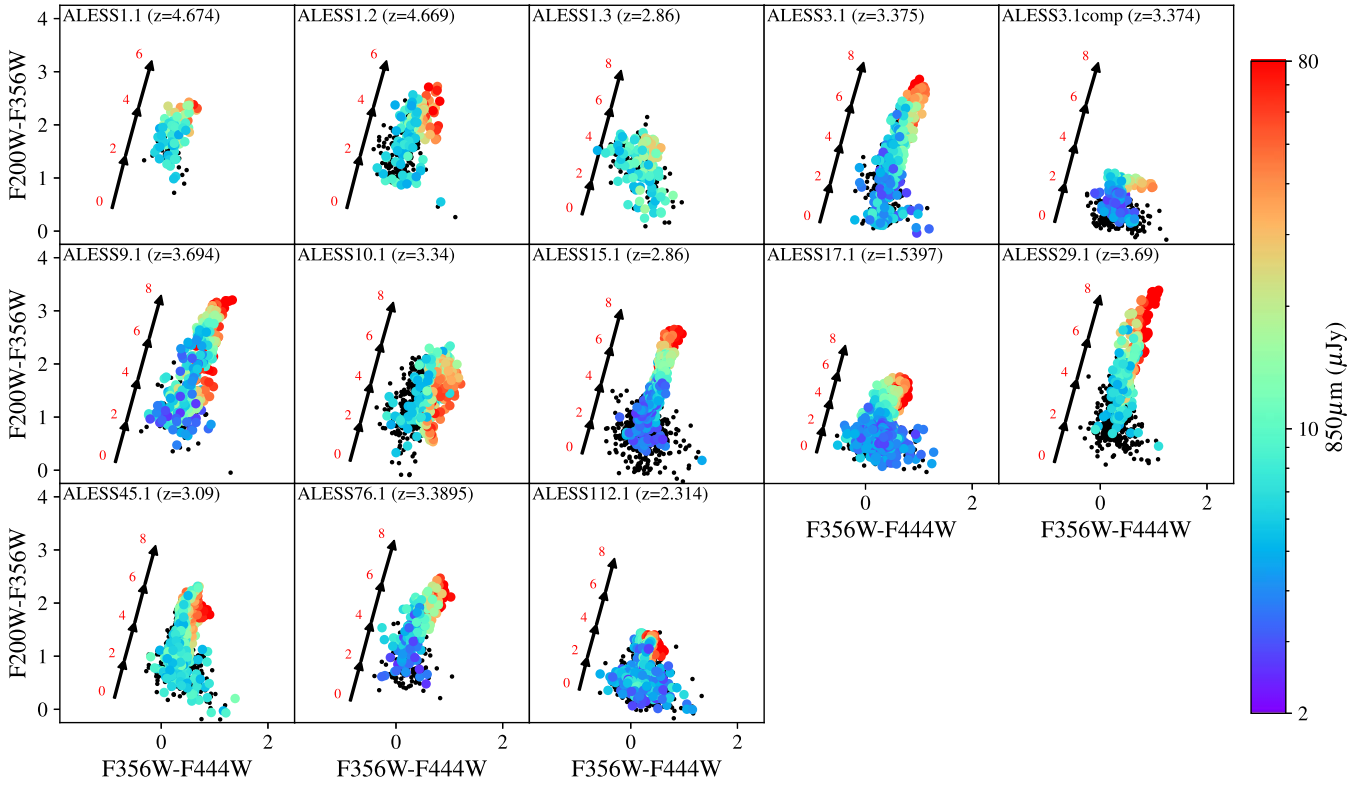

Figure 8. NIRCam color–color diagrams showing F200W–F356W vs. F356W–F444W colors for individual 60 × 60 mas regions within each galaxy with $>5\sigma$ detections in all three NIRCam filters. The data points are color-coded by their corresponding 870 μm flux surface density if the aperture has at least a 1σ detection in the ALMA 870 μm map; otherwise, the data points are colored black. Vectors indicating the predicted impact on this color space of varying A_V are shown for comparison and were obtained with MAGPHYS (E. da Cunha et al. 2008, 2015; see the text for details). The vectors are plotted with a shift 1 dex to the left for clarity. The majority of the sources show a correlation between redder NIRCam colors and 870 μm surface brightness.

ALMA 870 μm map; otherwise, the data points are colored black. In order to qualitatively assess the dust reddening properties in these sources, we also overplot vectors indicating the predicted impact on the colors of varying A_V. We emphasize that these vectors are not fits to the data, but rather were obtained using MAGPHYS spectral libraries (E. da Cunha et al. 2008, 2015) by finding the median color of stellar models within ± 0.1 dex of a given A_V value, shown from $A_V = 0$ to a maximum A_V that depends on redshift.

Figure 8 shows that for the majority of the sources, we see an extended distribution of points in the NIRCam color–color space, where the direction of the extension roughly matches that expected from the A_V vector. These distributions show that, as expected, the F200W–F356W color depends more strongly on A_V in the models than the F356W–F444W color (i.e., the vectors are closer to vertical than horizontal); this is due to the fact that dust attenuation affects shorter wavelengths more strongly than longer wavelengths. By comparing the observed distributions to these vectors, we find that the maximum A_V implied within each source on $\sim$1 kpc scales (for regions detected in F200W) ranges from $A_V < 4$ in ALESS 3.1-comp (which is the only source below the detection threshold of the original ALESS catalog) to $A_V \sim 8$ (in ALESS 9.1 and 29.1). For comparison, the median A_V of the ALESS sample from global spectral energy distribution (SED) fitting is only $A_V \sim 2$ mag (E. da Cunha et al. 2015).

Figure 8 also shows that for the majority of the sources, there is a correlation between redder NIRCam colors and 870 μm surface brightness; i.e., the chance of a point being bright at 870 μm is higher if it is red in both NIRCam colors. The clearest example of this correlation is seen in ALESS 15.1, but strong trends are also visible in ALESS 1.1, 1.2, 3.1, 9.1, 17.1, 29.1, 76.1, and 112.1 (and a weaker trend is visible in ALESS 1.3). This is a strong indicator that dust is the cause of the correlation.

Finally, we see that for some sources, there is a large variation in F200W–F356W color for a fixed F356W–F444W color and 870 μm surface brightness. ALESS 10.1 is the clearest example, but see also 1.2, 9.1, and 29.1. While ALESS 10.1 is visually classified as a merger/interaction, the appearance of this effect in the larger sample does not correlate with morphological classification (nor does it correlate with, e.g., F444W ellipticity). It is possible that this is due to a "frosting" of low-A_V (i.e., bluer) stars in front of the bulk of the higher-A_V emission. As a side effect, a dispersion in F356W–F444W color at a fixed F200W–F356W color is also introduced. The full implications of these diagrams for the distribution of stellar age, (dust-corrected) stellar mass, metallicity, and other derived parameters will be explored in J. Li et al. (2025, in preparation).

To further explore the general relation between dust in absorption and dust in emission, in Figure 9 we plot A_V versus dust mass surface density for our sources. Here the A_V values were derived by taking each pixel in the color–color diagram of Figure 8 with a $>1\sigma$ 870 μm flux density and projecting it onto the A_V vector at the source redshift (shown in Figure 8). To emphasize that these values are not fits to the data but purely empirical, we refer to this axis as A'_V in the figure. For the dust mass surface density, we use the calibration between 870 μm flux density and dust mass from U. Dudzevičiutė et al. (2020),

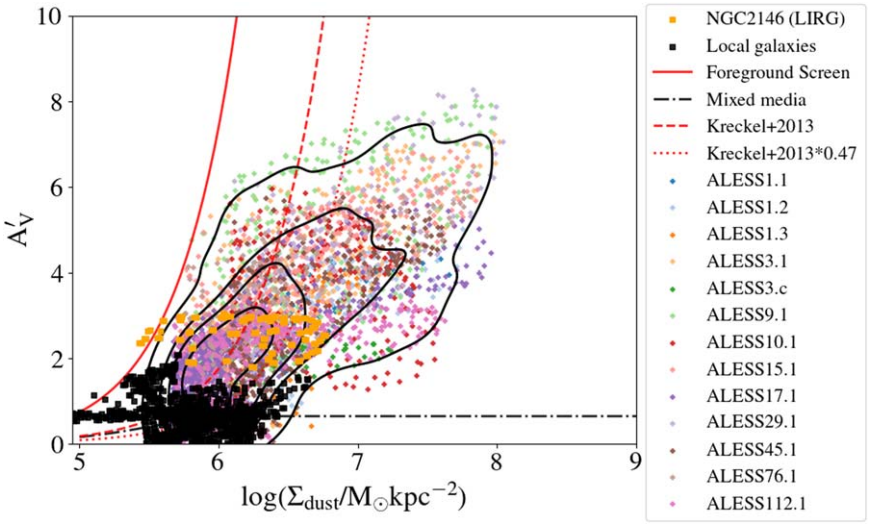

Figure 9. *V*-band extinction (inferred from the reddening of the stellar continuum) as a function of dust mass surface density for the 13 SMGs and a comparison sample of local galaxies from K. Kreckel et al. (2013). The black contours show the density of SMG data points, which are shown in different color circles for each galaxy. The local galaxies are shown as black squares, except for NGC 2146 (the only LIRG in the sample), which is shown as the orange squares. Overplotted are four lines: a foreground dust screen model (solid red line), a mixed media model (dotted–dashed black line), the empirical relation found by K. Kreckel et al. (2013) for nearby galaxies (dashed red line; see their Equation (8)), and the same relation scaled by a factor 0.47, as appropriate to convert from the reddening due to the Balmer decrement to that of the stellar continuum (dotted red line; K. Kreckel et al. 2013). The distribution and scatter seen for the SMGs are similar to those seen for local galaxies while extending the trend to higher dust mass surface densities. See Section 3.6 for further details.

where the dust masses were derived from MAGPHYS. We also compare to a sample of nearby galaxies from K. Kreckel et al. (2013) with A_V values derived from the reddening of the stellar continuum. Finally, we overplot four relations: the relation for a simple foreground dust screen between the emitter and absorber (based on the dust model from B. T. Draine & A. Li 2007 and using the dust-to-gas ratio from B. T. Draine et al. 2014); the relation for a mixed media model where stars and dust are uniformly mixed (from D. Calzetti et al. 2000, following K. Kreckel et al. 2013); the empirical relation established in K. Kreckel et al. (2013) for their local galaxies; and the same relation scaled by a factor 0.47 (dotted red line). The K. Kreckel et al. (2013) relation was determined on physical scales from 350 pc to 2 kpc, which is well matched to the scales probed here ($\sim$1 kpc), and it was derived by scaling the simple foreground dust screen model by a factor of $\sim$4 to account for geometric effects. While this relation (derived from the Balmer decrement) may already be appropriate for the current analysis given the similar A_V estimates for SMGs from stellar reddening and the Balmer decrement (E. J. Birkin 2022; D. Taylor et al. 2024, in preparation), we also show the relation scaled by an additional factor of 0.47 (as appropriate to convert from the reddening due to the Balmer decrement to that of the stellar continuum; K. Kreckel et al. 2013). These two relations should then bracket the behavior expected if the dust structure in our targets is similar to local galaxies.

Figure 9 shows that the relation between dust in absorption and dust in emission for the galaxies studied in this work broadly agrees with the trend reported for local galaxies, while also extending the trend to higher dust mass surface densities and *V*-band extinction. The scatter observed for the current targets also appears broadly consistent with that seen in the local sample, both between and within individual galaxies; in particular, we note that NGC 2146 (the only LIRG in the nearby sample) shows a similar spread to some of our sources. We discuss the additional implications of these findings in Section 4 below.

4. Discussion

4.1. The Influence of Dust on Rest-frame Optical/Near-infrared Morphologies

The JWST NIRCam images presented here reveal the bulk of the underlying stellar emission in these high-resolution ALMA-mapped submillimeter-selected galaxies. For this, observing at or beyond 3.5 μm (i.e., rest wavelength $\simeq$1 μm at $z \sim 3$) appears to be crucial. The morphologies can vary dramatically between F200W and F356W (i.e., between $\sim$0.5 and $\sim$1 μm rest-frame), with the majority of the sources appearing either barely detected or with suppressed central emission at F200W compared to F356W (Figure 2). However, at F356W, all sources are well detected, including several galaxies that were previously undetected in deep HST images at $\leqslant$1.6 μm (ALESS 1.1, 17.1, and 76.1; C.-C. Chen et al. 2015).

The correspondence for the majority of sources between the morphology of the NIRCam F444W and the matched-resolution 870 μm emission (particularly the peak positions and PAs) indicates that the spatial offsets previously reported between the 870 μm continuum and HST 1.6 μm emission (e.g., J. A. Hodge et al. 2012; C.-C. Chen et al. 2015; G. Calistro Rivera et al. 2018) were not due to true physical offsets, but rather that the morphologies inferred from the HST images were strongly affected by heavy structured dust obscuration, an effect also reproduced by radiative transfer modeling (R. K. Cochrane et al. 2019; G. Popping et al. 2022). For example, ALESS 29.1 was previously classified as a source with two separate stellar components, while four separate components were identified in ALESS 15.1 (C.-C. Chen et al. 2015). By uncovering the obscured centers of the underlying disks, the NIRCam images now clearly reveal that these "components" were simply due to differential dust obscuration in the disks. The higher A_V values in the galaxy centers (Figure 8) are thus causing the observed trend of larger effective radius at decreasing NIRCam wavelength (Figure 4).

We note that other studies have also reported spatial offsets between the rest-frame UV/optical stellar and interstellar medium (ISM) emission in a variety of high-redshift populations (e.g., C. Cheng et al. 2020; R. K. Cochrane et al. 2021; H. Inami et al. 2022; M. Killi et al. 2024), with various theories posited beyond dust geometry, including strong stellar feedback or large-scale gas inflow/outflows. While there may certainly be other mechanisms operating in different galaxy populations, we caution that—given the strong impact of dust demonstrated here up to $\simeq$1 μm (rest-frame)—structured dust obscuration should be ruled out before invoking more exotic explanations.

For some of the highest-redshift sources, we see strong evidence that the galaxies are still affected by significant dust obscuration even in the longest-wavelength (F444W) NIRCam filter. In particular, examining the F444W versus 870 μm continuum imaging for ALESS 1.1 ($z = 4.674$; Figure 3), as well as the comparison of the 870 μm map with the F444W GALFIT residuals (Figure 5), the dust continuum appears to align with a suppression in the intensity of the detectable stellar distribution, suggesting significant dust obscuration. This suppression in the central region of the F444W image likely explains the very low F444W-derived Sérsic index ($n = 0.36 \pm 0.04$). We note that we find a similarly low Sérsic index at F444W for our other $z > 4.5$ source, ALESS 1.2. In these sources, F444W is probing shorter rest-wavelength emission (780 nm rest-frame) that is more prone to dust extinction. For these particularly high-redshift/dusty sources, MIRI imaging will be important to more robustly characterize the stellar distributions.

4.2. Implications for Inclination Estimates

While some of the most basic morphological parameters show agreement between the 870 μm and F444W observations, others show no clear correlation (Figure 6). The most notable parameter showing a lack of correlation is the axis ratio (i.e., ellipticity). This lack of correlation has significant implications, as the ellipticity is used to set the inclination in the most simple but commonly used dynamical mass estimates (often even without error margins), with the tacit assumption that these are perfectly flat, infinitely thin, and perfectly circular disks. The lack of correlation between the ellipticities derived from different tracers shows that these inclinations are in fact very poorly determined, suggesting such dynamical mass estimates should be used with extreme caution.

4.3. Rest-frame Near-infrared versus Dust Continuum Sizes

The smaller extents measured for the ALMA 870 μm emission compared to those inferred from the F444W emission (Figure 4) suggests that the 870 μm emission is more weighted to the dusty centers of the sources. This is consistent with recent results inferred for JWST-observed SMGs compared with submillimeter continuum imaging of (largely) other samples (e.g., C.-C. Chen et al. 2022), but this study extends these results to direct comparisons of these tracers within the same galaxies. For sources without evidence for significant obscuration in the F444W filter, which could bias those size estimates to larger values, the smaller 870 μm continuum sizes measured here would suggest that these galaxies are still undergoing rapid morphological transformation, with the central starbursts likely building bulges that will eventually come to dominate the stellar mass distributions (for which the F444W filter serves only as a weak proxy). This result would strengthen the challenge these sources pose to recent hydrodynamical simulations, a number of which predict the opposite trend for galaxies in this stellar mass range (i.e., submillimeter extents that are larger than the stellar mass extents; e.g., R. K. Cochrane et al. 2019; G. Popping et al. 2022). Given the significant obscuration still present in even the longest-wavelength NIRCam images in at least some sources, this result needs to be tested via the creation of (dust-corrected) stellar mass maps (see I. Smail et al. 2023; J. Li et al. 2025, in preparation).

4.4. Evidence for Mergers and Interactions

While the NIRCam observations have now detected the dust-reddened centers of the galaxies—suggesting less irregular morphologies than implied from the heavily obscured 1.6 μm imaging (C.-C. Chen et al. 2015)—this does not imply that the galaxies all appear as undisturbed disks in F444W. On the contrary, the NIRCam images reveal evidence for mergers/interactions in the majority of the sources.

In particular, three of the SMGs have direct evidence for companions: ALESS 1.1 (with 1.2), ALESS 3.1, and ALESS 17.1. The most dramatic feature is the long tidal tail/stellar bridge that is now clearly visible between ALESS 1.1 and 1.2 at $z = 4.67$ (Figure 1). With a projected separation of $\sim$20 kpc and a velocity separation of $\sim$320 km s^{-1}, this suggests that ALESS 1.1 and 1.2 are undergoing an early-stage (violent) interaction. Interestingly, both sources are detected in CO(5-4) emission (J. E. Birkin et al. 2021), where ALESS 1.1 has a double-peaked profile with a very wide FWHM velocity width of 1300 km s^{-1}. This could indicate that ALESS 1.1 is itself a late-stage merger or that the gas disk is dynamically disturbed. With ALESS 1.3 lying in the same field—and showing evidence for two very close components, where the southern component is redder (Figure 2) and may be the primary source of its submillimeter emission (Figure 3)—this means that the original submillimeter source "LESS 1" (i.e., the brightest source in the original LABOCA "LESS" catalog, with $S_{850} = 14.5 \pm 1.2$ mJy; A. Weiß & K. Coppin 2009), was actually made up of at least two or more different and likely unrelated major merger events within its 19″ beam (FWHM). Meanwhile, while ALESS 3.1 and 3.1-comp are also likely undergoing an interaction, we note that ALESS 3.1 also has a broad (870 km s^{-1}) and asymmetric CO line profile (J. E. Birkin et al. 2021), potentially indicating that ALESS 3.1 itself is undergoing a late-stage interaction/merger. Thus, the original submillimeter source "LESS 3" (i.e., the third brightest source in the LESS catalog) also appears to consist of at least one or more mergers/interactions, implying that the brightest LESS (i.e., single-dish LABOCA) sources are mergers/interactions[40] (and see I. Mitsuhashi et al. 2021 for a discussion of an overdensity associated with the brightest SCUBA-2 source in COSMOS). This is a direct confirmation of trends reported previously based on the multiplicity of sources comprising bright single-dish-selected sources (e.g., S. M. Stach et al. 2018; J. M. Simpson et al. 2020).

The NIRCam images (and GALFIT residuals) also reveal evidence for interactions via features resembling stellar tidal

[40] We note that LESS 2 was not included in the high-resolution ALMA/JWST follow-up due to the sample selection.

tails/plumes and clumps in ALESS 10.1 and 76.1, as well as potential evidence in ALESS 9.1 and 112.1. Some of the apparent tidal features were previously detected in the dust continuum in the sources with the highest-resolution 870 μm emission maps (e.g., ALESS 3.1, 112.1; J. A. Hodge et al. 2019) and interpreted as either tidally induced spiral arms or the star-forming knots in an interaction/merger. ALESS 3.1 was already discussed above and indeed shows evidence of a merger/interaction also in the NIRCam images. With the new NIRCam imaging showing possible evidence of a warped disk (Figure 5), ALESS 112.1 may also be a late-stage merger. However, this case is less conclusive and is thus marked as Indeterminate. ALESS 9.1,[41] which also has a potential tidal feature detected in both NIRCam and 870 μm continuum (to its south), appears very clumpy in its rest-frame near-infrared emission, possibly due to an advanced interaction/merger with one of the nearby quiescent galaxies with similar photometric redshift (S. Alberts et al. 2024; though again marked "Indeterminate" due to the lack of clear evidence). In fact, of the 13 sources examined, only ALESS 15.1, 29.1, and 45.1 show no clear evidence in the current data for mergers/interactions, though we caution that these sources may still be late-stage mergers or interactions where the merger/interaction is less obvious due to projection effects or low-mass companions. We also point to the work of J. Vega-Ferrero et al. (2024), who suggest that visual classifications may overestimate disk fractions. Conversely, it should be noted that the departures from asymmetry used here to visually classify the galaxies as mergers/interactions in cases without a clear companion may also result from accretion from a cooling halo in gas-rich systems, which can be episodic and sporadic (e.g., J. Bland-Hawthorn et al. 2024).

Keeping these caveats in mind, the current interpretations result in a merger fraction of 54% $\pm$ 23% and a fraction of undisturbed disks of only 23% $\pm$ 8%—consistent (within the errors) with the larger but typically submillimeter-fainter sample of S. Gillman et al. (2024), who report 20% $\pm$ 5% candidate late-stage mergers plus 40% $\pm$ 10% potential minor mergers. Both our work and S. Gillman et al. (2024; as well as C.-C. Chen et al. 2022) imply higher merger fractions than reported for the mix of lensed and unlensed submillimeter sources studied by C. Cheng et al. (2023), but we caution that the current sample sizes are generally small and the visual classifications have large uncertainties that are difficult to quantify. Confirming these interpretations will ultimately require high-resolution kinematic data. However, regardless of their nature, the fact that a number of these (apparent tidal) features are also detected in the submillimeter continuum indicates that—despite the centrally concentrated 870 μm emitting regions—the high dust column densities and active star formation in these galaxies currently extends well beyond the existing central bulge, as we discuss further in Section 4.6.

4.5. Stellar Colors and the Structure of the ISM

One of the most notorious degeneracies in SED fitting is that between dust attenuation and stellar age, and this has long been a concern for SMG samples in particular (e.g., L. J. Hainline et al. 2011; M. J. Michałowski et al. 2014; U. Dudzevičiūtė et al. 2020). Although SED fitting that requires energy balance with the far-IR (FIR) emission can help by providing additional constraints on the dust attenuation (e.g., E. da Cunha et al. 2015), the assumptions behind this energy balance have not been thoroughly tested in the high-redshift Universe. In particular, the dust model used in such SED-fitting codes is calibrated based on the Milky Way (e.g., B. T. Draine & A. Li 2007) and may not be applicable beyond the local Universe and/or in extreme starbursts.

With this in mind, the relations seen in Figures 8 and 9 are notable. In particular, the correlation between NIRCam colors and 870 μm surface brightness seen for the majority of the sources (Figure 8) implies that the primary driver behind the red stellar colors in these SMGs is *dust* rather than stellar age. Figure 9 further implies that the dust-to-stellar distributions in these SMGs are similar (on the same $\sim$kpc scales) to those in nearby star-forming galaxies, particularly the LIRG NGC 2146, which exhibits similar A_V for gas and stars (as also seen in high-redshift SMGs; E. J. Birkin 2022; D. Taylor et al. 2024, in preparation). The bulk of the SMG data points fall in a similar regime between the foreground dust screen and mixed media models as the K. Kreckel et al. (2013) relation, indicating a similar correction factor to the foreground-screen model is applicable for these $z \sim 3$ sources as found at $z \sim 0$. This suggests that the ISM in these galaxies consists of a similar combination of mixed dust and emitting material and foreground-screen components (see N. Tomičić et al. 2017 for a higher-resolution study in M31), with the remaining scatter likely due to geometric effects and nonuniformity in the dust distribution on scales beneath our resolution.

At low dust mass surface densities ($<10^6$ $M_\odot$ kpc^{-2}), it is noteworthy that the SMG data points remain below the limit set by the dust screen model despite the NIRCam data's sensitivity to higher A_V values. This suggests that this simple model—based on Milky Way–like dust—remains valid for these $z \sim 3$ sources. Meanwhile, at the highest dust mass surface densities probed by these data ($\gtrsim 10^7$–10^8 $M_\odot$ kpc^{-2}), the K. Kreckel et al. (2013) relation would predict A_V values up to $\sim$100 mag, far in excess of what we measure. However, for these particularly high-density regions, our measured A_V values likely correspond to lower limits due to the maximum optical depth to the stellar continuum emission that we can detect with NIRCam. Given that the nearby galaxies used to calibrate the K. Kreckel et al. (2013) relation did not sample such high dust mass surface densities, this does not affect our conclusions.

In summary, the ISM structure in these SMGs appears largely similar to local star-forming galaxies on $\sim$kpc scales. This similarity implies that some of the most basic assumptions that go into SED-fitting codes such as, e.g., MAGPHYS (i.e., the dust model) are still valid for these $z \sim 3$ galaxies.

4.6. Rest-frame Near-infrared and Gas/dust Bars

Lastly, we discuss the potential presence of bars in the sources. As discussed in detail in J. A. Hodge et al. (2019) and seen in Figure 3, there are elongated, bar-like substructures in the 870 μm images of some of the targets, which J. A. Hodge et al. (2019) interpret as dust bars (see, W. Rujopakarn et al. 2019). While bars are often associated with secular evolution due to their tendency to arise naturally in dynamically cool disk galaxies (e.g., E. Athanassoula & J. A. Sellwood 1986), they can also be efficiently triggered by interactions (J. E. Barnes & L. E. Hernquist 1991; T. J. Cox et al. 2008; P. F. Hopkins et al. 2009) and thus are not mutually exclusive with the tidal/merger

[41] We note that ALESS9.1 from J. A. Hodge et al. (2013) is also cataloged in JADES as 172813 (S. Alberts et al. 2024).

signatures observed here in a large fraction of the sample. Bars are also consistent with the most recent theoretical expectations for gas-rich galaxies at high-redshift: Though previous work on bar formation found that the presence of (inert) gas reduces a stellar bar's lifetime (J. Villa-Vargas et al. 2010) or weakens the bars that form (E. Athanassoula et al. 2013), more recent work using hydrodynamic *N*-body simulations to predict bar formation in gas-rich disks at high redshift has found that turbulent gas *accelerates* bar formation, predicting bar-like phenomena even in fully gas-dominated turbulent disks (J. Bland-Hawthorn et al. 2024). Finally, bars can also be an important mechanism to systematically drive gas inward in sources with no current evidence for mergers/interaction, helping to explain the intense dusty star formation (and possibly supermassive black hole growth).

Given the high A_V values implied in the center of these sources, it is perhaps not surprising that we see no evidence for strong bars in the rest-frame near-infrared images presented here, as the stellar components could easily be hidden behind the high implied dust columns. Another possible (but more speculative) explanation comes from the work of J. Bland-Hawthorn et al. (2024), who predicted that as the gas fraction increases, the role of any stellar bar becomes less important, with mostly gas bars emerging via radial shear flows in galaxies with the highest gas fractions. Considering the high gas fractions inferred for these sources (e.g., A. M. Swinbank et al. 2014), it is thus possible that their stellar bars are weaker than those in less gas-dominated sources. In either scenario, these dust-rich structures would necessarily be young. Notably, J. Bland-Hawthorn et al. (2024) found that the bars formed in the most gas-rich disks collapse to form bulges after $\sim$1.5 Gyr, which would then imply that the bar-like features observed in these sources are an immediate precursor to further significant bulge growth. Ultimately, larger samples of sources covering a range of submillimeter flux densities as well as high-resolution kinematic data will be necessary to determine the importance of gas/dust and/or stellar bars in the mass assembly of the general SMG population.

5. Conclusions

We have presented JWST NIRCam imaging of 13 $z \sim 3$ submillimeter-selected galaxies that have uniquely deep, high-resolution (0.″08–0.″16) ALMA 870 μm imaging, which previously mapped their dust disks on $\sim$0.5–1 kpc scales. Our main findings are as follows:

1. All of the sources are securely detected by the JWST NIRcam imaging, including several galaxies that were previously undetected in deep HST 1.6 μm images. For this, observing at or beyond $\sim$3.5 μm ($\simeq$1 μm rest-frame at $z \sim 3$) appears to be crucial, as the morphologies of the sources vary dramatically between F200W and F356W (i.e., between $\sim$0.5 μm and $\sim$1 μm rest-frame).
2. With the dust-reddened galaxy centers now more visible, the newly revealed rest-frame near-infrared morphologies show some clear similarities to the 870 μm dust continuum images (specifically the position angles and peaks), demonstrating that the spatial offsets previously reported between the 870 μm and HST morphologies were due to strong differential dust obscuration.
3. However, we find no correlation between the axis ratio (i.e., ellipticity) derived from the rest-frame near-infrared and 870 μm dust continuum. As the ellipticity is commonly used to set the inclination in dynamical mass estimates, this lack of correlation shows that these inclinations are in fact very poorly determined and that resulting dynamical mass estimates should be used with extreme caution.
4. In some sources (particularly those at the highest redshifts), we see convincing evidence that the galaxies are still affected by significant dust obscuration even in the longest-wavelength (F444W) NIRCam filter. For these particularly dusty/high-redshift sources, MIRI imaging will be crucial to more robustly characterize the stellar distributions.
5. Due to the high level of central obscuration in the galaxies, we find that the median effective radius of the galaxies systematically decreases with increasing NIRCam wavelength. We nevertheless find that the F444W sizes are still 78 $\pm$ 21% larger than those measured at 870 μm. Thanks to the unique depth and resolution of the 870 μm images available for these targets, this strengthens the challenge posed to recent hydrodynamical simulations claiming the opposite trend (R. K. Cochrane et al. 2019; G. Popping et al. 2022). However, given the significant obscuration still present in even the longest-wavelength NIRCam filter in at least some of the sources, this result needs to be tested via the creation of stellar mass maps (J. Li et al. 2025, in preparation).
6. The NIRCam imaging reveals clear evidence for mergers/interactions (e.g., tidal tails/plumes) in the majority of the sources, with 54 $\pm$ 23% visually classified as mergers/interactions, 23 $\pm$ 31% classified as indeterminate, and only 23 $\pm$ 8% appearing as undisturbed disks (though we caution that these interpretations may miss late-stage mergers or be affected by episodic gas accretion from cooling halos). Several of the (apparently tidal) features are also detected in 870 μm emission, indicating that the active star formation in these galaxies currently extends well beyond the existing central bulges.
7. We find a clear correlation between redder NIRCam colors and 870 μm surface brightness on $\sim$ 1 kpc scales. This is a strong indicator that the SMGs have red NIRCam colors due to dust rather than stellar age. We further show that the relation between dust in absorption and dust in emission for the galaxies studied in this work is broadly similar to the trend seen in nearby star-forming galaxies. This suggests that the ISM structure on $\sim$ kpc scales in these $z \sim 3$ galaxies is similar to that in $z \sim 0$ sources.
8. We find no evidence for strong bars in our targets in the rest-frame near-infrared. This suggests that the elongated bar-like structures seen in the high-resolution 870 μm images are highly dust-obscured and/or gas-rich and thus young, implying they are the immediate precursors to further significant bulge growth.

Taken together, these findings suggest we are witnessing heavily obscured and largely interaction-induced bulge formation events at the centers of these massive star-forming galaxies. The present study thus demonstrates the joint power of JWST and ALMA for uncovering the morphologies and likely formation histories of high-redshift dusty galaxies. Future work will incorporate the multiwavelength data into resolved SED fitting to explore the resolved physical properties, stellar masses, and

resolved kinematics (J. Li et al. 2025, in preparation; B. Westoby et al. 2025, in preparation). Combined with future large samples of sources covering a range of submillimeter flux densities, such studies will be crucial to shed further light on the dominant mechanisms governing the mass assembly of massive, dusty galaxies at high redshift and the relation of these sources to the larger high-redshift galaxy population.

Acknowledgments

We thank the anonymous referee and Joss Bland-Hawthorn for feedback on the manuscript. J.H. and B.W. acknowledge support from the ERC Consolidator grant 101088676 ("VOYAJ"). E.d.C. and J.L. acknowledge support from the Australian Research Council (projects DP240100589 and CE170100013). A.M.S. and I.R.S. acknowledge STFC (ST/X001075/1). C.C.C. acknowledges support from the National Science and Technology Council of Taiwan (111-2112M-001-045-MY3), as well as Academia Sinica through the Career Development award (AS-CDA-112-M02). R.D. acknowledges support from the INAF GO 2022 grant "The birth of the giants: JWST sheds light on the buildup of quasars at cosmic dawn" and by the PRIN MUR "2022935STW," RFF M4.C2.1.1, CUP J53D23001570006 and C53D23000950006. T.R.G. acknowledge funding from the Cosmic Dawn Center (DAWN), funded by the Danish National Research Foundation (DNRF) under grant DNRF140. K.K. acknowledges support from the Knut and Alice Wallenberg Foundation. M.R. is supported by the NWO Veni project "Under the lens" (VI.Veni.202.225).

This work is based in part on observations made with the NASA/ESA/CSA James Webb Space Telescope. The data were obtained from the Mikulski Archive for Space Telescopes at the Space Telescope Science Institute, which is operated by the Association of Universities for Research in Astronomy, Inc., under NASA contract NAS 5-03127 for JWST. These observations are associated with program No. 2516. The specific observations analyzed can be accessed via doi:10.17909/e33v-ga73. Support for program No. 2516 was provided by NASA through a grant from the Space Telescope Science Institute, which is operated by the Association of Universities for Research in Astronomy, Inc., under NASA contract NAS 5-03127. S.K. acknowledges advice and support from Anton Koekemoer, Armin Rest, and Pablo Perez Gonzalez for the reduction of NIRCam data.

This paper makes use of the following ALMA data: ADS/JAO.ALMA#2016.1.00048.S, ADS/JAO.ALMA#2012.1.00307.S, and ADS/ JAO.ALMA#2011.1.00294.S. ALMA is a partnership of ESO (representing its member states), NSF (USA), and NINS (Japan), together with NRC (Canada) and NSC and ASIAA (Taiwan) and KASI (Republic of Korea), in cooperation with the Republic of Chile. The Joint ALMA Observatory is operated by ESO, AUI/NRAO, and NAOJ.

The Hubble Source Catalog is based on data from the Hubble Legacy Archive, which is a collaboration between the Space Telescope Science Institute (STScI/NASA), the Space Telescope European Coordinating Facility (ST-ECF/ESAC/ESA), and the Canadian Astronomy Data Centre (CADC/NRC/CSA).

This research made use of ASTROPY, a community developed core Python package for astronomy (Astropy Collaboration et al. 2013, 2018; Collaboration Astropy et al. 2022) hosted at http://www.astropy.org/, matplotlib (J. D. Hunter 2007), NUMPY (S. van der Walt et al. 2011), SCIPY (Virtanen et al. 2020), and of TOPCAT (M. B. Taylor 2005). This research also made use of PHOTUTILS, an Astropy package for detection and photometry of astronomical sources (L. Bradley et al. 2022).

Appendix
Additional Tables and Figures

Table 3 shows the astrometric accuracy we estimate for each of the NIRCam pointings. Both relative and absolute accuracy are indicated, as well as the number of Gaia stars (with catalog proper motions) available for the absolute astrometric alignment.

Figure 10 shows the cumulative fraction of integrated flux density versus radius in each of the three NIRCam filters for the targeted SMGs (including 3.1-comp, and excluding 17.1 due to confusion with its optically bright companion). The corresponding curve for the highest-resolution 870 μm image available for each source is also shown. These curves are not deconvolved from their (respective) PSFs, but this has a minor effect given that the sources are well resolved. A curve corresponding to the F444W PSF, which has the lowest resolution of the NIRCam filters, is shown as an example.

Table 3
NIRCam Final Astrometric Alignment Accuracy

Pointing	No. GAIA Sources	Relative Accuracy[a] (mas)	Absolute Accuracy (mas)	Catalog
1	2	11	65	Gaia DR3
2	8	13	34	Gaia DR3
3	5	10	19	Gaia DR3
4	4	15	20	Gaia DR3

Note.
[a] Relative accuracy is measured between F200W/F356W/F444W filters.

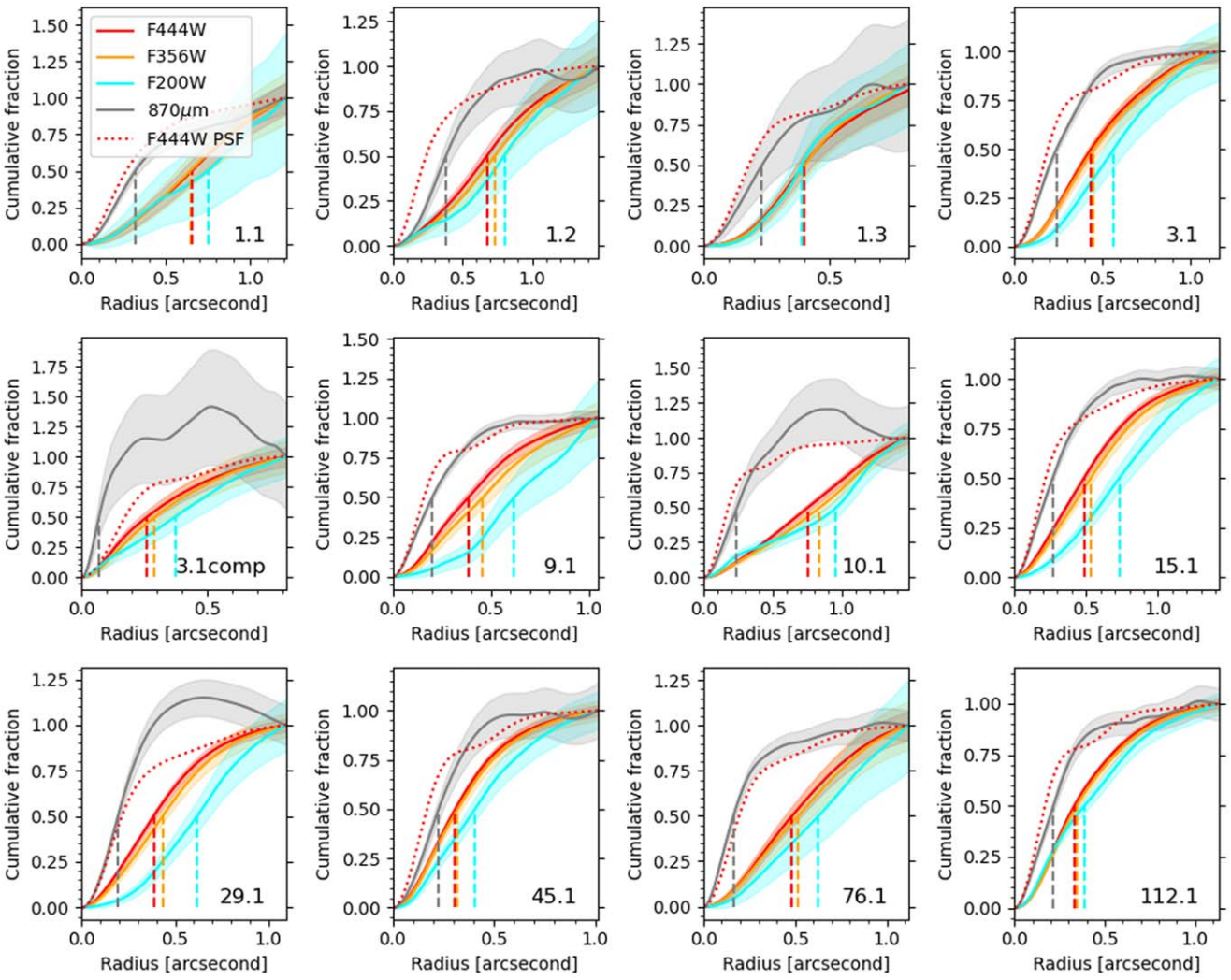

Figure 10. Cumulative fraction of integrated flux density in JWST NIRCam and ALMA 870 μm vs. radius along the major axis for the targeted SMGs (including 3.1-comp, and excluding 17.1 due to confusion with its optically bright companion). The dotted line indicates the PSF in the F444W filter. The dashed lines indicate the effective radius in each filter, which we find to generally decrease with increasing NIRCam wavelength in these galaxies. Note that the curve corresponding to 870 μm may stray above 1.0 or even decrease with radius due to the presence of noise in the ALMA imaging, indicated by the gray-toned band (representing $\pm 1\sigma$). In the majority of the sources, the effective radius decreases with increasing NIRCam wavelength, and the effective radius of the ALMA 870 μm emission is more compact than that from even the reddest JWST NIRCam filter.

ORCID iDs

J. A. Hodge https://orcid.org/0000-0001-6586-8845
E. da Cunha https://orcid.org/0000-0001-9759-4797
S. Kendrew https://orcid.org/0000-0002-7612-0469
J. Li https://orcid.org/0000-0002-8184-5229
I. Smail https://orcid.org/0000-0003-3037-257X
B. A. Westoby https://orcid.org/0009-0004-3732-6394
O. Nayak https://orcid.org/0000-0001-6576-6339
A. M. Swinbank https://orcid.org/0000-0003-1192-5837
C.-C. Chen https://orcid.org/0000-0002-3805-0789
F. Walter https://orcid.org/0000-0003-4793-7880
P. van der Werf https://orcid.org/0000-0001-5434-5942
M. Cracraft https://orcid.org/0000-0002-7698-3002
A. Battisti https://orcid.org/0000-0003-4569-2285
W. N. Brandt https://orcid.org/0000-0002-0167-2453
G. Calistro Rivera https://orcid.org/0000-0003-0085-6346
S. C. Chapman https://orcid.org/0000-0002-8487-3153
P. Cox https://orcid.org/0000-0003-2027-8221
H. Dannerbauer https://orcid.org/0000-0001-7147-3575
R. Decarli https://orcid.org/0000-0002-2662-8803
M. Frias Castillo https://orcid.org/0000-0002-9278-7028
T. R. Greve https://orcid.org/0000-0002-2554-1837
K. K. Knudsen https://orcid.org/0000-0002-7821-8873
S. Leslie https://orcid.org/0000-0002-4826-8642
K. M. Menten https://orcid.org/0000-0001-6459-0669
M. Rybak https://orcid.org/0000-0002-1383-0746
E. Schinnerer https://orcid.org/0000-0002-3933-7677
J. L. Wardlow https://orcid.org/0000-0003-2376-8971
A. Weiss https://orcid.org/0000-0003-4678-3939

References

Alberts, S., Williams, C. C., Helton, J. M., et al. 2024, ApJ, 975, 85
Algera, H. S. B., Inami, H., Oesch, P. A., et al. 2023, MNRAS, 518, 6142
Algorry, D. G., Navarro, J. F., Abadi, M. G., et al. 2017, MNRAS, 469, 1054
Amvrosiadis, A., Lange, S., Nightingale, J., et al. 2024, arXiv:2404.01918
Astropy Collaboration, Price-Whelan, A. M., Lim, P. L., et al. 2022, ApJ, 935, 167
Astropy Collaboration, Price-Whelan, A. M., Sipőcz, B. M., et al. 2018, AJ, 156, 123

Astropy Collaboration, Robitaille, T. P., Tollerud, E. J., et al. 2013, A&A, 558, A33
Athanassoula, E., Machado, R. E. G., & Rodionov, S. A. 2013, MNRAS, 429, 1949
Athanassoula, E., & Sellwood, J. A. 1986, MNRAS, 221, 213
Bagley, M. B., Finkelstein, S. L., Koekemoer, A. M., et al. 2023, ApJL, 946, L12
Barger, A. J., Cowie, L. L., Sanders, D. B., et al. 1998, Natur, 394, 248
Barger, A. J., Wang, W.-H., Cowie, L. L., et al. 2012, ApJ, 761, 89
Barnes, J. E., & Hernquist, L. E. 1991, ApJL, 370, L65
Baugh, C. M., Lacey, C. G., Frenk, C. S., et al. 2005, MNRAS, 356, 1191
Bertin, E., & Arnouts, S. 1996, A&AS, 117, 393
Birkin, J. E. 2022, PhD thesis, Durham Univ.
Birkin, J. E., Weiss, A., Wardlow, J. L., et al. 2021, MNRAS, 501, 3926
Bland-Hawthorn, J., Tepper-Garcia, T., Agertz, O., & Federrath, C. 2024, ApJ, 968, 86
Boogaard, L. A., Gillman, S., Melinder, J., et al. 2024, ApJ, 969, 27
Bouwens, R., González-López, J., Aravena, M., et al. 2020, ApJ, 902, 112
Bradley, L., Sipocz, B., Robitaille, T., et al. 2022, astropy/photutils: v1.5.0, Zenodo, doi:10.5281/zenodo.6825092
Bushouse, H., Eisenhamer, J., Dencheva, N., et al. 2023, JWST Calibration Pipeline, v1.10.2, Zenodo, doi:10.5281/zenodo.7829329
Calistro Rivera, G., Hodge, J. A., Smail, I., et al. 2018, ApJ, 863, 56
Calzetti, D., Armus, L., Bohlin, R. C., et al. 2000, ApJ, 533, 682
Cardamone, C. N., van Dokkum, P. G., Urry, C. M., et al. 2010, ApJS, 189, 270
Casey, C. M., Narayanan, D., & Cooray, A. 2014, PhR, 541, 45
Cathey, J., Gonzalez, A. H., Lower, S., et al. 2024, ApJ, 967, 11
Chabrier, G. 2003, PASP, 115, 763
Chen, C.-C., Smail, I., Swinbank, A. M., et al. 2015, ApJ, 799, 194
Chen, C.-C., Harrison, C. M., Smail, I., et al. 2020, A&A, 635, A119
Chen, C.-C., Gao, Z.-K., Hsu, Q.-N., et al. 2022, ApJL, 939, L7
Cheng, C., Ibar, E., Smail, I., et al. 2020, MNRAS, 499, 5241
Cheng, C., Huang, J.-S., Smail, I., et al. 2023, ApJL, 942, L19
Cimatti, A., Cassata, P., Pozzetti, L., et al. 2008, A&A, 482, 21
Cochrane, R. K., Hayward, C. C., Anglés-Alcázar, D., et al. 2019, MNRAS, 488, 1779
Cochrane, R. K., Best, P. N., Smail, I., et al. 2021, MNRAS, 503, 2622
Colina, L., Crespo Gómez, A., Álvarez-Márquez, J., et al. 2023, A&A, 673, L6
Cox, T. J., Jonsson, P., Somerville, R. S., Primack, J. R., & Dekel, A. 2008, MNRAS, 384, 386
Crespo Gómez, A., Colina, L., Álvarez-Márquez, J., et al. 2024, arXiv:2402.18672
da Cunha, E., Charlot, S., & Elbaz, D. 2008, MNRAS, 388, 1595
da Cunha, E., Walter, F., Smail, I. R., et al. 2015, ApJ, 806, 110
Danielson, A. L. R., Swinbank, A. M., Smail, I., et al. 2017, ApJ, 840, 78
Debattista, V. P., & Sellwood, J. A. 2000, ApJ, 543, 704
Draine, B. T., & Li, A. 2007, ApJ, 657, 810
Draine, B. T., Aniano, G., Krause, O., et al. 2014, ApJ, 780, 172
Dudzevičiūtė, U., Smail, I., Swinbank, A. M., et al. 2020, MNRAS, 494, 3828
Eales, S., Lilly, S., Gear, W., et al. 1999, ApJ, 515, 518
Gaia Collaboration, Vallenari, A., Brown, A. G. A., et al. 2023, A&A, 674, A1
Gillman, S., Gullberg, B., Brammer, G., et al. 2023, A&A, 676, A26
Gillman, S., Smail, I., Gullberg, B., et al. 2024, A&A, 691, A299
Gullberg, B., Smail, I., Swinbank, A. M., et al. 2019, MNRAS, 490, 4956
Guo, Y., Jogee, S., Finkelstein, S. L., et al. 2023, ApJL, 945, L10
Hainline, L. J., Blain, A. W., Smail, I., et al. 2011, ApJ, 740, 96
Hauser, M. G., Arendt, R. G., Kelsall, T., et al. 1998, ApJ, 508, 25
Hayward, C. C., Behroozi, P. S., Somerville, R. S., et al. 2013a, MNRAS, 434, 2572
Hayward, C. C., Narayanan, D., Kereš, D., et al. 2013b, MNRAS, 428, 2529
Hill, R., Chapman, S. C., Scott, D., et al. 2018, MNRAS, 477, 2042
Hodge, J. A., Carilli, C. L., Walter, F., et al. 2012, ApJ, 760, 11
Hodge, J. A., & da Cunha, E. 2020, RSOS, 7, 200556
Hodge, J. A., Karim, A., Smail, I., et al. 2013, ApJ, 768, 91
Hodge, J. A., Swinbank, A. M., Simpson, J. M., et al. 2016, ApJ, 833, 103
Hodge, J. A., Smail, I., Walter, F., et al. 2019, ApJ, 876, 130
Hopkins, P. F., Cox, T. J., Younger, J. D., & Hernquist, L. 2009, ApJ, 691, 1168
Hopkins, P. F., Hernquist, L., Cox, T. J., et al. 2006, ApJS, 163, 1
Huang, S., Kawabe, R., Kohno, K., et al. 2023, ApJL, 958, L26
Hughes, D. H., Serjeant, S., Dunlop, J., et al. 1998, Natur, 394, 241
Hunter, J. D. 2007, CSE, 9, 90
Ikarashi, S., Kohno, K., Aguirre, J. E., et al. 2011, MNRAS, 415, 3081
Ikarashi, S., Ivison, R. J., Caputi, K. I., et al. 2015, ApJ, 810, 133
Inami, H., Algera, H. S. B., Schouws, S., et al. 2022, MNRAS, 515, 3126
Iono, D., Peck, A. B., Pope, A., et al. 2006, ApJL, 640, L1
Jogee, S., Barazza, F. D., Rix, H.-W., et al. 2004, ApJL, 615, L105
Kamieneski, P. S., Frye, B. L., Pascale, M., et al. 2023, ApJ, 955, 91
Karim, A., Swinbank, A. M., Hodge, J. A., et al. 2013, MNRAS, 432, 2
Killi, M., Ginolfi, M., Popping, G., et al. 2024, MNRAS, 531, 3222
Kreckel, K., Groves, B., Schinnerer, E., et al. 2013, ApJ, 771, 62
Lang, P., Schinnerer, E., Smail, I., et al. 2019, ApJ, 879, 54
Lovell, C. C., Geach, J. E., Davé, R., Narayanan, D., & Li, Q. 2021, MNRAS, 502, 772
Luo, B., Brandt, W. N., Xue, Y. Q., et al. 2017, ApJS, 228, 2
Lyu, J., Alberts, S., Rieke, G. H., & Rujopakarn, W. 2022, ApJ, 941, 191
Marinova, I., & Jogee, S. 2007, ApJ, 659, 1176
Martinez-Valpuesta, I., Shlosman, I., & Heller, C. 2006, ApJ, 637, 214
Mather, J. C. 1994, InPhT, 35, 331
McAlpine, S., Smail, I., Bower, R. G., et al. 2019, MNRAS, 488, 2440
McKinney, J., Finnerty, L., Casey, C. M., et al. 2023, ApJL, 946, L39
Menéndez-Delmestre, K., Sheth, K., Schinnerer, E., Jarrett, T. H., & Scoville, N. Z. 2007, ApJ, 657, 790
Michałowski, M. J., Hayward, C. C., Dunlop, J. S., et al. 2014, A&A, 571, A75
Mitsuhashi, I., Matsuda, Y., Smail, I., et al. 2021, ApJ, 907, 122
Narayanan, D., Hayward, C. C., Cox, T. J., et al. 2010, MNRAS, 401, 1613
Narayanan, D., Turk, M., Feldmann, R., et al. 2015, Natur, 525, 496
Neugebauer, G., Habing, H. J., van Duinen, R., et al. 1984, ApJL, 278, L1
Peng, C. Y., Ho, L. C., Impey, C. D., & Rix, H.-W. 2002, AJ, 124, 266
Peng, C. Y., Ho, L. C., Impey, C. D., & Rix, H.-W. 2010, AJ, 139, 2097
Perrin, M. D., Sivaramakrishnan, A., Lajoie, C.-P., et al. 2014, Proc. SPIE, 9143, 91433X
Planck Collaboration, Aghanim, N., Akrami, Y., et al. 2020, A&A, 641, A6
Popping, G., Pillepich, A., Calistro Rivera, G., et al. 2022, MNRAS, 510, 3321
Puget, J. L., Abergel, A., Bernard, J. P., et al. 1996, A&A, 308, L5
Rieke, M. J., Kelly, D. M., Misselt, K., et al. 2023, PASP, 135, 028001
Rodriguez-Gomez, V., Snyder, G. F., Lotz, J. M., et al. 2019, MNRAS, 483, 4140
Rujopakarn, W., Daddi, E., Rieke, G. H., et al. 2019, ApJ, 882, 107
Sanders, D. B., & Mirabel, I. F. 1996, ARA&A, 34, 749
Sheth, K., Elmegreen, D. M., Elmegreen, B. G., et al. 2008, ApJ, 675, 1141
Simpson, J. M., Swinbank, A. M., Smail, I., et al. 2014, ApJ, 788, 125
Simpson, J. M., Smail, I., Swinbank, A. M., et al. 2015, ApJ, 799, 81
Simpson, J. M., Smail, I., Swinbank, A. M., et al. 2017, ApJ, 839, 58
Simpson, J. M., Smail, I., Dudzevičiūtė, U., et al. 2020, MNRAS, 495, 3409
Smail, I., Chapman, S. C., Blain, A. W., & Ivison, R. J. 2004, ApJ, 616, 71
Smail, I., Ivison, R. J., & Blain, A. W. 1997, ApJL, 490, L5
Smail, I., Dudzevičiūtė, U., & Gurwell, M. 2023, ApJ, 958, 36
Smolčić, V., Aravena, M., Navarrete, F., et al. 2012, A&A, 548, A4
Spilker, J. S., Marrone, D. P., Aravena, M., et al. 2016, ApJ, 826, 112
Stach, S. M., Smail, I., Swinbank, A. M., et al. 2018, ApJ, 860, 161
Stach, S. M., Dudzevičiūtė, U., Smail, I., et al. 2019, MNRAS, 487, 4648
Swinbank, A. M., Chapman, S. C., Smail, I., et al. 2006, MNRAS, 371, 10673
Swinbank, A. M., Smail, I., Chapman, S. C., et al. 2010, MNRAS, 405, 234
Swinbank, A. M., Simpson, J. M., Smail, I., et al. 2014, MNRAS, 438, 1267
Targett, T. A., Dunlop, J. S., Cirasuolo, M., et al. 2013, MNRAS, 432, 2012
Taylor, M. B. 2005, in ASP Conf. Ser. 347, Astronomical Data Analysis Software and Systems XIV, ed. P. Shopbell, M. Britton, & R. Ebert (San Francisco, CA: ASP), 29
Toft, S., SmolÄić, V., Magnelli, B., et al. 2014, ApJ, 782, 68
Tomičić, N., Kreckel, K., Groves, B., et al. 2017, ApJ, 844, 155
van der Walt, S., Colbert, S. C., & Varoquaux, G. 2011, CSE, 13, 22
van der Wel, A., Bell, E. F., Häussler, B., et al. 2012, ApJS, 203, 24
van der Wel, A., Martorano, M., Häußler, B., et al. 2024, ApJ, 960, 53
van Dokkum, P. G., Franx, M., Kriek, M., et al. 2008, ApJL, 677, L5
Vega-Ferrero, J., Huertas-Company, M., Costantin, L., et al. 2024, ApJ, 961, 51
Villa-Vargas, J., Shlosman, I., & Heller, C. 2010, ApJ, 719, 1470
Wang, S. X., Brandt, W. N., Luo, B., et al. 2013, ApJ, 778, 179
Virtanen, P., Gommers, R., Oliphant, T. E., et al. 2020, NatMe, 17, 261
Wang, W.-H., Cowie, L. L., Barger, A. J., & Williams, J. P. 2011, ApJL, 726, L18
Wang, W.-H., Cowie, L. L., van Saders, J., Barger, A. J., & Williams, J. P. 2007, ApJL, 670, L89
Weiß, A., Kovács, A., Coppin, K., et al. 2009, ApJ, 707, 1201
Wozniak, H., Friedli, D., Martinet, L., Martin, P., & Bratschi, P. 1995, A&AS, 111, 115
Younger, J. D., Dunlop, J. S., Peck, A. B., et al. 2008, MNRAS, 387, 707
Younger, J. D., Fazio, G. G., Huang, J.-S., et al. 2009, ApJ, 704, 803
Zavala, J. A., Casey, C. M., Manning, S. M., et al. 2021, ApJ, 909, 165